Geochemistry Geophysics Geosystems G3
AN ELECTRONIC JOURNAL OF THE EARTH SCIENCES
Published by AGU and the Geochemical Society

Article
Volume 3, Number 9
20 September 2002
8602, doi:10.1029/2001GC000247
ISSN: 1525-2027

Seismic anisotropy in the upper mantle 2. Predictions for current plate boundary flow models

Donna K. Blackman and J.-Michael Kendall

Scripps Institution of Oceanography, 8602 La Jolla Shores Drive, La Jolla, California 92037, USA (dblackman@ucsd.edu)

Department of Earth Sciences, University of Leeds, Leeds LS2 9JT, UK (kendall@earth.leeds.ac.uk)

[1] The anisotropic seismic structure due to flow-induced mineral alignment is investigated for a series of models designed to simulate deformation in the upper mantle within a few hundred kilometers of a plate boundary. The orientation distributions of olivine:enstatite aggregates evolve along streamlines of each flow model, based on each grains plastic response to the local stress/strain field. The effective elastic tensor for these textured aggregates provides predictions of *P* wave anisotropy and shear wave splitting throughout the model space. *P* and *S* travel time delay patterns and fast shear wave polarization angles are found to vary significantly with incidence angle for a given model. Comparison of predicted fast *P* direction for our method versus a finite-strain based estimate shows that agreement is acceptable for much of the model space, but notable differences occur in regions up to several tens of kilometers in size. Two-dimensional models of spreading center flow are presented for slow and fast rates and for several cases in which the ridge migrates over the deeper mantle. The effect of flow in the third dimension is addressed in a few calculations. For one comparison of flow in the mantle wedge at a subduction zone, the introduction of trench parallel flow causes significant changes in the predicted patterns of *P* wave anisotropy (magnitude, more than orientation) and SKS splitting.

Components: 10,560 words, 15 figures.

Keywords: Anisotropy; mantle convection; mid-ocean ridge; subduction; East Pacific Rise; mineral preferred orientation.

Index Terms: 5120 Physical Properties of Rocks: Plasticity, diffusion, and creep; 7218 Seismology: Lithosphere and upper mantle; 3035 Marine Geology and Geophysics: Midocean ridge processes; 8150 Tectonophysics: Evolution of the Earth: Plate boundary—general 3040.

Received 1 October 2001; **Revised** 30 April 2002; **Accepted** 10 May 2002; **Published** 20 September 2002.

Blackman, D. K., and J.-M. Kendall, Seismic anisotropy in the upper mantle, 2, Predictions for current plate boundary flow models, *Geochem. Geophys. Geosyst.*, *3*(9), 8602, doi:10.1029/2001GC000247, 2002.

Theme: The Oman Ophiolite and Mid-Ocean Ridge Processes
Guest Editor: Peter Kelemen, Chris MacLeod and Susumu Umino

1. Introduction

[2] The potential for using measurements of seismic anisotropy to determine the pattern of flow in the upper mantle has been known for a few decades [*Hess*, 1964; *Nicolas and Poirier*, 1976; *Forsyth*, 1975; *McKenzie*, 1979; *Nishimura and Forsyth*, 1989; *Ribe*, 1989, 1992; *Silver*, 1996], but recent improvements in seismic instrumentation and computational capabilities provide new impetus for more detailed models of mineral alignment in polycrystalline peridotite and determination of the seismic experiments required for discerning deformation patterns in regions of complex flow. This is most relevant in the vicinity of plate boundaries where the spatial scale of variability in the deformation field is of the order of tens to a few hundred kilometers. Gradients in deformation across a tectonic boundary and changes in the along-strike boundary geometry or plate motion can generate anisotropic structure that varies significantly, in both azimuthal and vertical planes, on a regional scale. Our aim is to illustrate the nature of variability that could arise from physically reasonable changes in flow/deformation parameters and to show how predictions from these more complete models compare with previous simpler estimates of the symmetry of the anisotropy.

[3] The full physical system is rather complex, so simplifications are often made when inferring the relationship between measures of the degree of seismic anisotropy, its orientation, and the mantle deformation at depth. For example, it is commonly assumed that olivine "fast direction" is aligned either horizontally or vertically and parallel to a large-scale flow direction [*Forsyth*, 1975; *Shimamura*, 1984; *Shearer and Orcutt*, 1985; *Nishimura and Forsyth*, 1989; *Silver and Chan*, 1991]. Far from plate boundaries this approach probably provides reasonable inferences [*Ribe*, 1989]. However, our results indicate a number of situations in which the relationship between fast *P* wave propagation and the polarization directions and degree of the shear wave splitting need to be characterized in a more robust manner for reliable inferences about mantle deformation to be made.

[4] We use a "lower bound" method to simulate the development of texture in upper mantle rocks [*Chastel et al.*, 1993; *Dawson and Wenk*, 1999]. This approach does not account for explicit grain-grain interaction, and it favors stress equilibrium over strain compatibility between grains. The self-consistent method [*Wenk et al.*, 1991] compromises between stress equilibrium and strain compatibility, so it provides more accurate responses in situations where strain hardening occurs, for example. However, this improved capability comes at considerable computational expense compared with the lower bound method. *Tommasi et al.* [2000] showed that the elastic constants computed for lower bound and self-consistent texture predictions agree quite well. Thus we are able to have reasonable confidence in our predictions of how anisotropic seismic structure varies as a function of the style of upper mantle flow near plate boundaries.

2. Symmetric, Two-Dimensional Spreading Center Flow Models

2.1. Finite Strain Versus Direct Texture Estimates of Anisotropy

[5] Olivine preferred orientations in deformed laboratory samples have been related to the direction of finite strain in several studies [reviews by *Nicolas and Poirier*, 1976; *Carter*, 1976; *Nicolas and Christensen*, 1987; *Ribe*, 1992]. *McKenzie* [1979] reviewed how the deformation rate tensors for general flow fields are used to determine the finite strain that a material volume experiences. For some simple flow fields, he used the general correspondence between the orientations of finite strain ellipses and the nature of anisotropy determined in early seismic experiments [*Raitt et al.*, 1969; *Forsyth*, 1975] to support the approach of using finite strain as a proxy for the orientation of upper mantle flow-induced anisotropy. *Ribe* [1989, 1992] and *Ribe and Yu* [1991] developed a more detailed model of olivine orientation distributions. *Ribe* [1992] showed that the direction of seismic anisotropy should coincide with finite strain when texture development is well described by the ellipse rotation, but constraints on the relationship between the magnitude of the anisotropy and the finite strain ellipse elongation were

found to be less robust. A number of recent studies [e.g., *Toomey et al.*, 2002; *Hall et al.*, 2000] use finite strain to estimate the orientation of the anisotropic symmetry axis in the upper mantle. *Hall et al.* [2000] discuss how shear wave splitting parameters based on direct models of texture development, and the corresponding elastic constants, compare to estimates based on finite strain orientations and the elastic constants of a naturally deformed peridotite. In section 5 we elaborate on those results for both two-dimensional (2-D) and three-dimensional (3-D) subduction flow models. In this section, we comment on some general aspects of finite strain versus direct texture calculations in the estimation of flow-induced seismic anisotropy.

[6] We present results for passive and buoyancy-enhanced spreading center flow models since their different strain fields provide a good illustration of when finite strain ellipses are a useful proxy for the nature of seismic anisotropy and when this approach breaks down. Details of the direct texture calculation method are discussed in a companion paper [*Blackman et al.*, 2002] as well as in earlier publications [*Chastel et al.*, 1993; *Blackman et al.*, 1996]. The passive and buoyancy-enhanced models presented by *Blackman et al.* [1996] are updated to include texturing of 70:30 olivine:enstatite aggregates rather than pure olivine. Aggregates with random orientation distribution begin texturing at depths of 200 km, a depth that is expected to be in the range of depths where dislocation creep becomes the dominant deformation mechanism [*Karato*, 1992]. The aggregate is tracked along streamlines and texture is calculated at 1% strain increments. The *a* axis pole figures for these models are quite similar to those in our previous paper [*Blackman et al.*, 1996, 2002, Figure 10], but now the tendency toward horizontal alignment at the previously-used 100 km model base is reduced.

[7] We use Voigt-Reuss-Hill averages to obtain effective elastic constants employed for modeling wave propagation in the textured, 1000-grain aggregates of our model. Individual grain contributions are derived from single crystal constants [*Anderson and Isaak*, 1995; *Kumazawa*, 1969], which are projected according to each crystals calculated orientation. Temperature and pressure derivatives of the individual elastic constants are not included in the results shown throughout this paper since they do not change the results significantly. *Mainprice et al.* [2000] note that the change in degree of anisotropy is altered by only a couple percent in the upper mantle when these terms are included. We confirmed this by testing several elastic tensors for various model positions presented in this paper. More importantly for most of our discussion, the fast *P* directions and shear wave splitting patterns were not significantly altered when *T* and *P* derivatives were included for the elastic constant estimates.

[8] The finite strain ellipses for the passive flow model (Figure 1a) do a good job of matching the orientation of olivine *a* axis maxima that are reflected in the fast *P* directions shown by the vectors in Figure 1b (and by pole figures by *Blackman et al.* [2002], Figure 10). Not only is the change in orientation within and just below the lithosphere captured, but a reduction of ellipse elongation is also indicated. This is due to the change in principal extension direction from subvertical, corresponding to upwelling, to subhorizontal, associated with plate spreading. The reduced ellipse elongation is accompanied by a randomization of texture in the full calculation as aggregates pass beyond the turning point in the flow.

[9] The buoyant model is characterized by generally high finite strain levels even in the lithosphere and subplate regions. There is general agreement in the upwelling region between the finite strain ellipse size and orientation and the textures shown by the *a* axis pole figures. However, in the off-axis regions (beyond $\sim$50 km from the spreading center) the finite strain and texture results diverge. In the upper 80 km, the finite strain ellipse does not account for the bipolar texture with its associated reduction in strength of anisotropy. In contrast to the passive flow case, the influence of the plate spreading strain does not counteract previously developed subvertical strain accumulated in the upwelling zone. This is partly due to the greater vertical strain associated with high upwelling rates in the buoyant case and partly a reflection of the

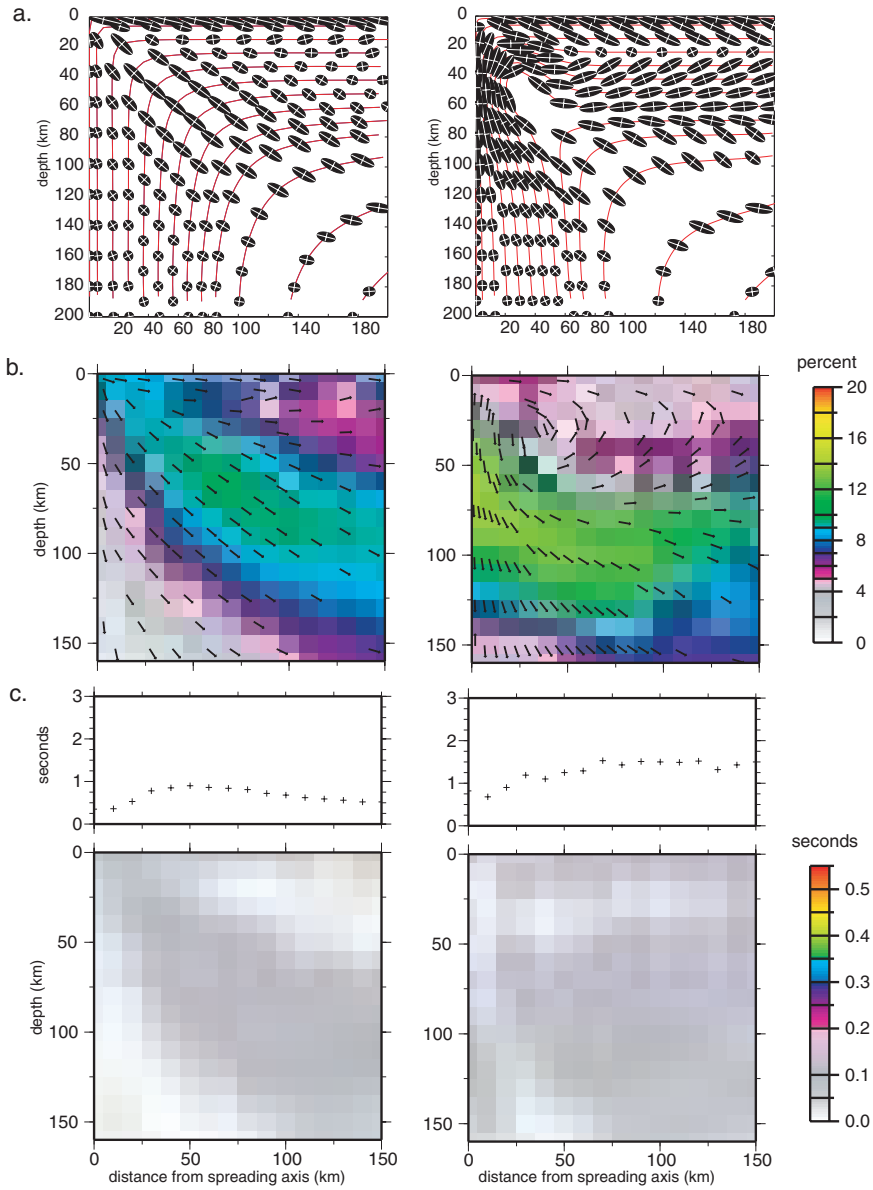

Figure 1. Symmetric two-dimensional (2-D) plate spreading flow for passive model (left column) and buoyancy-enhanced model (right column). (a) Finite strain ellipses all have unit length minor axis and the length of the major axis illustrates strain elongation experienced by material volumes moving along a streamline. An elongated ellipse can become equiaxed if strain in one direction is overcome by subsequent strain in a new direction and vorticity is low. (b) *P* wave anisotropy in the plane of the model. Color shade indicates degree of anisotropy and vectors show direction of fastest *P* propagation. (c) Shear wave splitting for vertical incidence. Depth section (below) illustrates the regions in the model where splitting accrues (split times assume 10 km propagation distance, the size of a pixel). Top panel shows splitting that would be measured at the surface after propagation through the 200 km deep model.

more complex flow that focuses towards the axis to supply the rapid upflow.

[10] We calculate the degree of *P* wave anisotropy, and the amount of shear wave splitting in the plane of the model for each aggregates position. This illustrates the anisotropic structure encountered by body waves traveling perpendicular to the plate boundary. There can be additional complexity for waves traveling at azimuths out of this plane [*Blackman et al.*, 2002] but here we focus on the in-plane structure for comparison with finite strain. The effective elastic constants are used to compute *P* wave velocity and the difference in the two

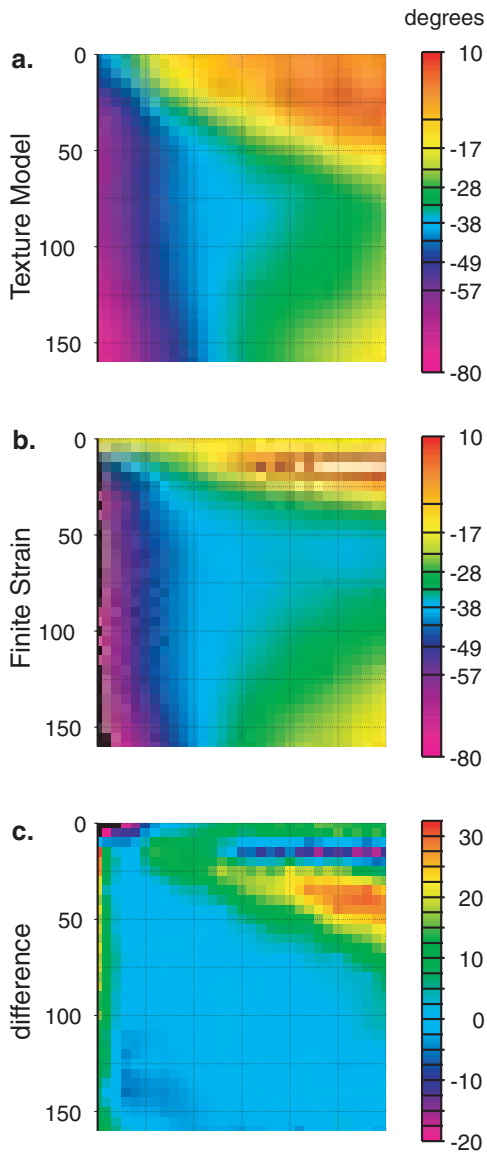

Figure 2. Comparison of predicted fast *P* wave directions for the passive, slow-spreading flow model. (a) Orientations (relative to horizontal) for the full texture calculation. (b) Orientations based on finite strain ellipse. (c) Difference between Figures 2a and 2b.

quasi-shear wave speeds at every incidence angle from 0 to 180 degrees (vertical, upgoing to vertical, downgoing, with 90 degrees being horizontal) in steps of 2°. The incidence angle of the maximum *P* wave speed is recorded for that position along the streamline. Since we calculate texture along streamlines, it is computationally efficient to simply output textures at a set number of strain increments along the flow line. This results in unevenly spaced elastic constants, but as long we consider sufficiently dense streamlines, we can accurately display the variations in anisotropy. (For cases where full wave propagation is modeled, we make the extra effort of calculating textures and elastic constants for many more streamlines whose endpoints are evenly spaced.) Unevenly spaced values of percent *P* wave anisotropy are gridded using a surface fitting algorithm with tension [*Smith and Wessel*, 1990]. The gridded values are displayed with color indicating the magnitude and vectors show the orientations (at subsampled, unevenly spaced positions; Figure 1b). Gridded values of the local SKS splitting are shown in Figure 1c; the sum of the accrued delay is plotted above the grids.

[11] Comparison of the elongation of the finite strain ellipses (Figure 1a) and the color shades of Figure 1b suggests that the anisotropic *P* wave structure of the passive flow model can usefully be illustrated with finite strain, whereas the structure of the buoyant flow model is not as well captured. The ellipse orientations match the fast *P* vectors in the lower and left portion of the buoyant model fairly well, but in the upper 50 km, not only do the orientations compare poorly, the finite strain does not predict the reduction in degree of effective anisotropy. In Figure 2, a more quantitative comparison is shown for the passive flow model. Differences of 20°–30° in predicted fast *P* direction occur in a region below the lithosphere that thickens with distance off axis where the degree of anisotropy is calculated to be 5–8%. Throughout the rest of the model space, the finite strain and full texture models predict fast *P* directions that agree to within 5°–10°, the limit of typical measurement accuracy.

2.2. Dependence on Incidence Angle

[12] There are clear differences in the petrofabrics and anisotropy at depth in the passive and buoyancy-enhanced spreading flow models, but it is important to assess the degree to which seismic waves propagating through these structures accrue diagnostic signatures that will be recorded at the Earth's surface. Asymptotic ray theory [*Guest and Kendall*, 1993] provides a good illustration of the integrated travel time (including any ray bending as estimated for a high frequency simulation) and shear wave splitting effects of the anisotropic

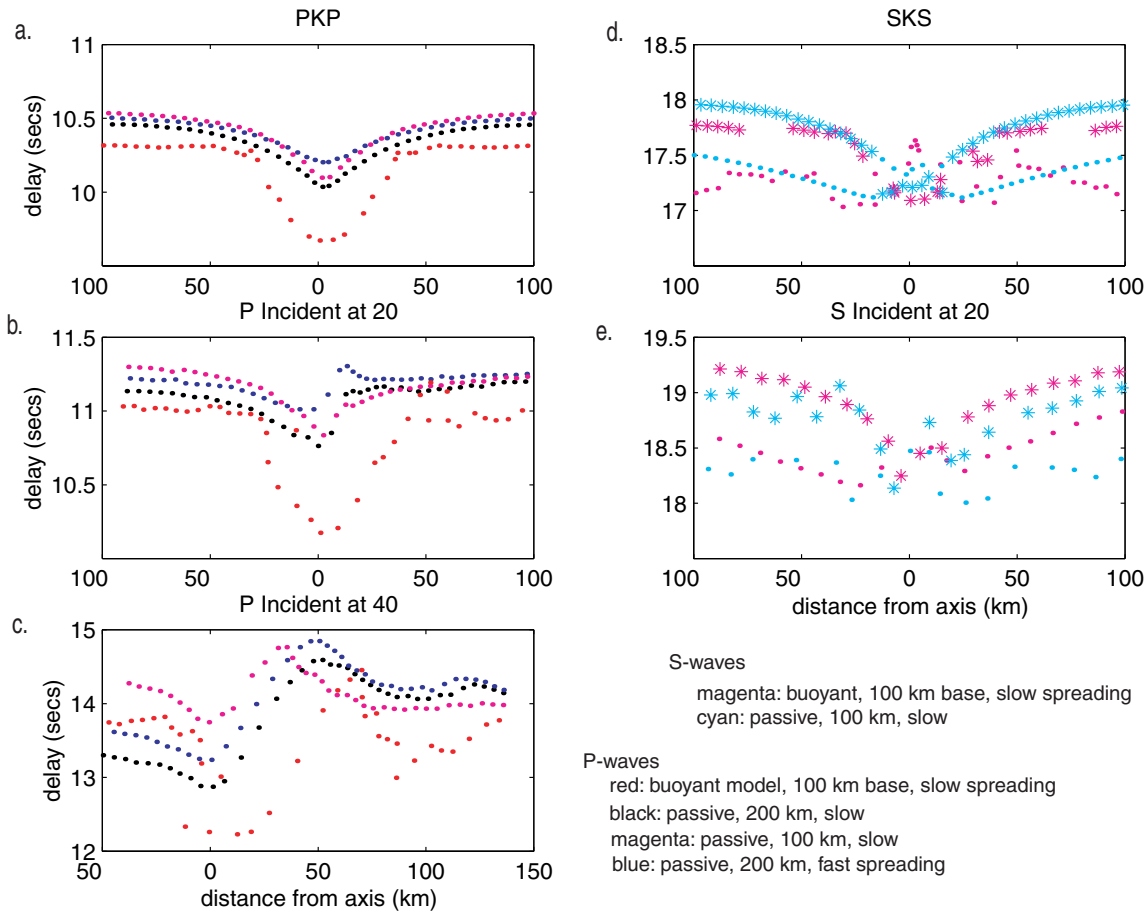

Figure 3. Travel time anomalies predicted by modeling propagation of body waves at various incidence angles through the passive and buoyancy-enhanced spreading center anisotropy models. (a) Vertically incident *P* waves (PKP) for the various models (see legend). (b) *P* waves incident at 20°, arriving from the west. (c) *P* waves incident at 40°, arriving from the west. (d) Vertically incident *S* waves (SKS) for two slow-spreading models. The fast shear wave and slow shear waves are indicated by different symbols and the symbol color corresponds to the model. (e) *S* waves incident at 20°, arriving from the west, for the models in Figure 3d.

models. We compare a series of spreading center textural anisotropy models where the following parameters are varied: asthenosphere viscosity (i.e., passive versus buoyant flow); depth at which texturing begins (100 and 200 km); spreading rate (slow and fast).

[13] The pattern of the predicted travel time anomalies and shear wave splitting depends significantly on the incidence angle of the seismic wave. Figure 3a compares *P* wave arrival times for the various models at vertical incidence (PKP), and these results are similar to what we have shown previously [*Blackman et al.*, 1996, 2002]. The symmetric axial travel time advance ranges from 0.25 to 0.75 s and is due to the concentrations of subvertically aligned *a* axes within the aggregates. When the incidence angle is increased, the travel time anomaly is no longer symmetric about the spreading axis. For a wave arriving at 20° from the west, an axial travel time advance persists, but the trough is narrower and asymmetric. For the fast spreading case, a small delay is predicted at the eastern ridge flank a short distance off axis (Figure 3b). A similar but more accentuated pattern is predicted for a wave arriving at 40° incidence from the west (Figure 3c). The largest compressional wave anomalies are predicted for the buoyancy-enhanced model. In contrast to the case of vertical wave propagation, the difference between the cases where the texturing starts at 200

versus 100 km become very significant as the propagation angle increases.

[14] Travel times for the fast and slow shear waves propagating vertically and at an angle of 20° in the passive and buoyant 70:30 olivine:enstatite models are shown in Figures 3d–3e. The off-axis splitting is slightly larger for the buoyancy enhanced case than for the passive case, but the difference would probably not be above the noise in seafloor seismic data. This contrasts with the results of *Blackman et al.* [1996] where models comprised entirely of olivine generally showed much larger off-axis splitting and the buoyancy-enhanced case showed twice as much off-axis splitting as the passive olivine model (2 s versus 1 s). In the off-axis regions the shear wave polarized perpendicular to the ridge axis propagates more quickly than the shear wave polarized parallel to the ridge axis. The opposite is true directly above the ridge axis, but the degree of splitting is much smaller and doubtfully observable in real data.

[15] The polarization of the fastest shear wave can vary with incidence angle. For the passive flow model, at near-vertical incidence the local fast shear wave is polarized parallel to the direction of spreading throughout essentially the whole region. Only directly below the axis is the polarization predicted to parallel the strike of the ridge and this region is too narrow (<3 km) to contribute to a signal that would be observed at the seafloor. The zone of axis-parallel polarization increases size for 20° incidence, with a downward-widening wedge whose base extends almost 50 km off-axis. Elsewhere, the polarizations are spreading-parallel. The pattern for 40° incidence is striking; only in the lithosphere are fast *S* polarizations predicted to parallel the flow direction. The asthenosphere fast *S* polarizations are all ridge-parallel.

3. Migrating, Asymmetric Spreading Center Flow Models

[16] The predicted pattern of upper mantle flow beneath an oceanic spreading center varies not only with assumed viscosity structure of the asthenosphere [*Sleep and Rosendahl*, 1979; *Sotin and Parmentier*, 1989; *Buck and Su*, 1989; *Turcotte and Phipps Morgan*, 1992; *Blackman et al.*, 1996; J. A. Conder et al., Asthenospheric flow and the asymmetry of the East pacific Rise, MELT area, manuscript submitted to *Journal of Geophysical Research*, 2001, hereinafter referred to as Conder et al., submitted manuscript, 2001; *Toomey et al.*, 2002] but also with spreading rate, symmetry of plate motion and direction of any migration of the ridge over the deeper mantle [*Stein et al.*, 1977; *Davis and Karsten*, 1986; *Blackman*, 1997]. The flow models discussed so far had constant asthenospheric viscosity, slow, symmetric plate spreading, and no migration of the ridge. We have already shown that body wave signatures are resolvably different for the passive and buoyancy-enhanced slow spreading cases. In this section we investigate a series of models that are motivated by seismic data collected during the MELT experiment on the fast-spreading southern East Pacific Rise (EPR) [*Forsyth et al.*, 1998b]. We show that the anisotropic structure at depth can vary significantly between models and several aspects of the predicted surface signatures are detectably different.

[17] The average spreading rate at 17°S on the EPR is 73 mm/yr and the ridge migrates ~32 mm/yr to the west. Asymmetric upper mantle structure is indicated in several types of geophysical data: rates of seafloor deepening away from the axis, Bouguer gravity anomaly, off-axis volcanic activity, and seismic signature [*Rea*, 1975; *Cochran*, 1986; *Forsyth et al.*, 1998a; *Scheirer et al.*, 1998; *Toomey et al.*, 1998; *Forsyth,* 1998a; *Wolfe et al.,*, 1998]. All suggest the west side has higher mantle temperature, perhaps associated with flow from the Pacific superswell region.

3.1. Reference Migrating Ridge Model

[18] A useful reference model is a fast-spreading, migrating ridge in which the asthenosphere flows passively in response to motion of the plates. Similar to the slow-spreading cases, the lithosphere thickens in proportion to the square root of plate age and is essentially rigid. Here we use an asthenospheric viscosity of 5×10^{19} Pa s. Far from the ridge, the side velocity boundary conditions follow the analytic solution for corner flow (300 km from

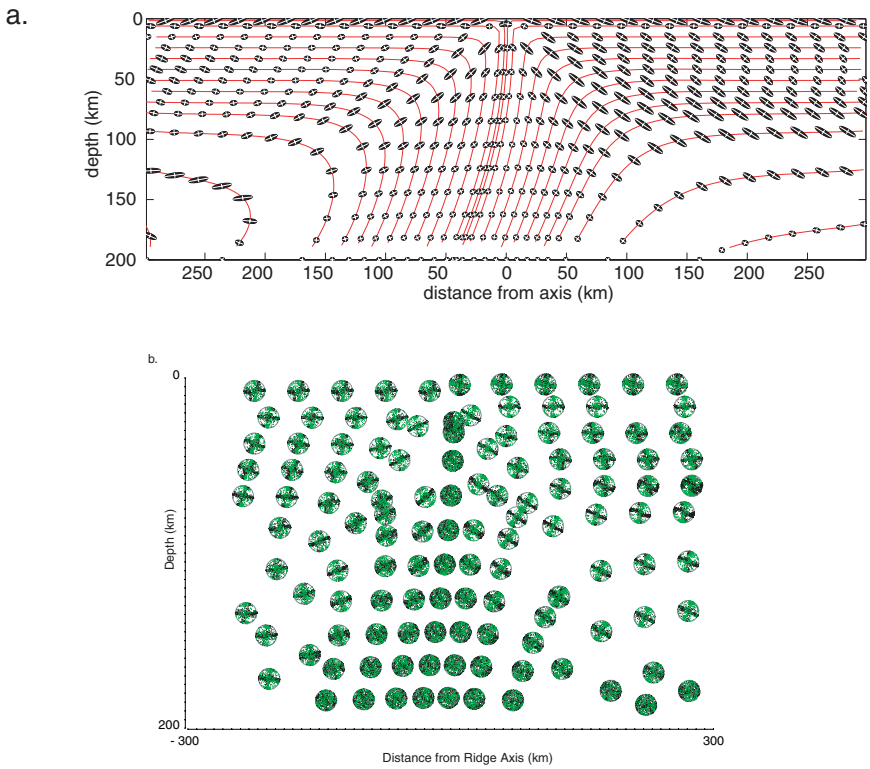

Figure 4. Reference fast-spreading, migrating spreading center model. (a) Streamlines and finite strain ellipses (see Figure 1 caption). (b) The *a* axis pole figures for olivine (70%, black)/enstatite (30%, green) aggregates. (c) *P* wave anisotropy in the plane of the model. (d) Maximum shear wave splitting in each local 20 km region (pixel size). The ray path that accrues this amount of splitting varies with position and is shown by the black vector. (e) Minimum shear wave splitting in each local region with corresponding path shown by vector. Compare with Figure 4d to see strong dependence of shear wave splitting on incidence angle. (f) Amount of splitting for vertically incidence shear waves. Lower panel shows local values and upper panel integrates these to determine the splitting that would be measured at the surface. Color scales for Figures 4c–4f are the same as in Figure 1.

the ridge axis). At the base of the model (250 km), ridge migration is simulated by imposing a horizontal velocity of 32 mm/yr to the east (the deep mantle flows east in a ridge reference frame). Vertical flow at the base is allowed to adjust as necessary to conserve mass in the model space. Streamlines and finite strain ellipses for this flow field are shown in Figure 4a. The calculated textures are shown by *a* axis pole figures for a 70:30 olivine:enstatite aggregate. Initial orientation distributions are random and texturing begins at 200 km depth. The overall pattern in the (100) pole figures (Figure 4b) is similar to a symmetric passive flow case, but east-west differences are evident upon inspection of the upper ~80 km. As the finite strain ellipses indicate, the deformation history that aggregates ending up below the eastern ridge flank experience is rather different than that experienced by aggregates that end up beneath the western flank. Although there is asymmetry in the upwelling region, the anisotropic structure beneath the spreading axis is not very different than for a symmetric case since textures are not strong for this model.

[19] Variations in the anisotropic structure associated with this texture model are shown in Figures 4c and 4d for rays traveling in the spreading-parallel plane. The degree of *P* wave anisotropy and the orientation of the fastest propagation direction are shown in Figure 4c. The west side of the model is characterized by higher degrees of anisotropy, but the direction of fastest *P* wave propagation is not very different from corresponding positions on the east side. The orientations of the fast *P* directions are fairly similar to the finite strain ellipse orientations, but the sense of the asymmetry in *P* aniso-

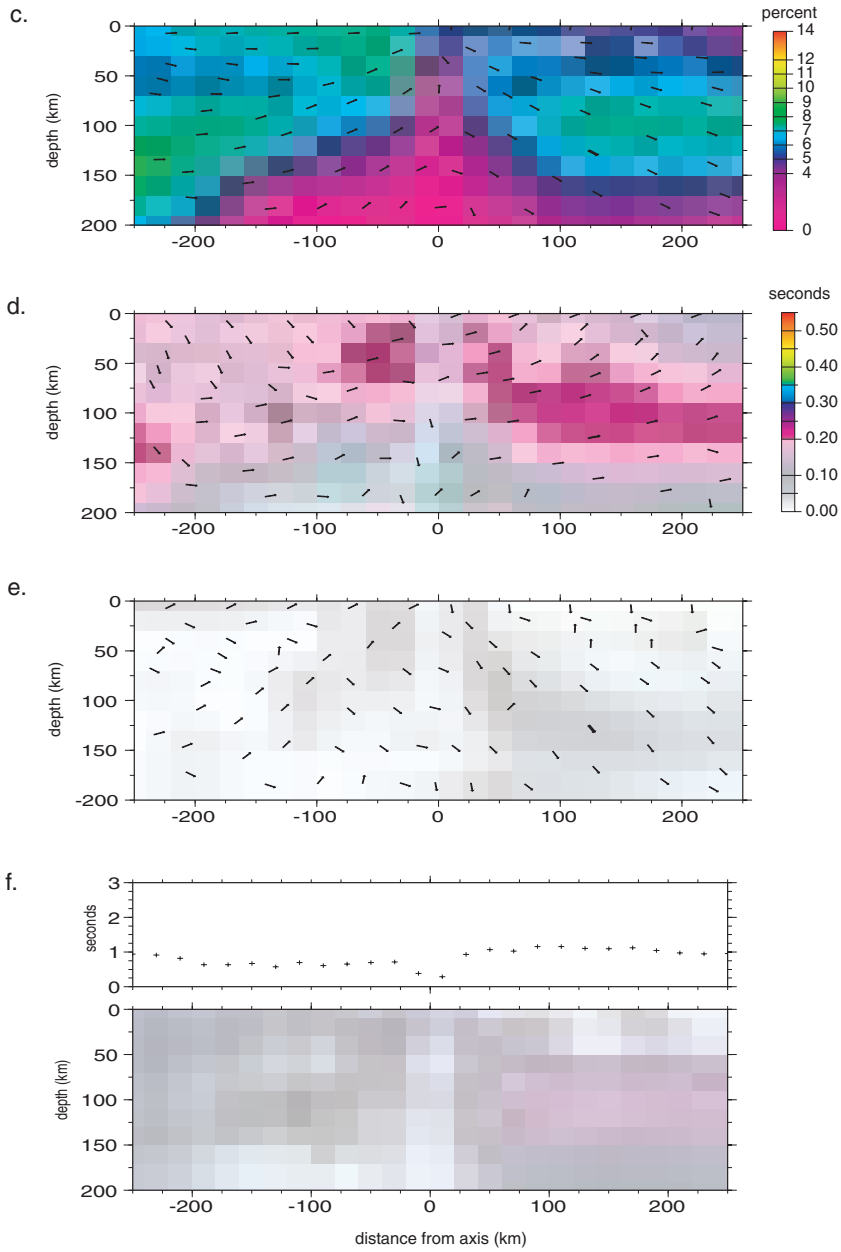

Figure 4. (continued)

tropy magnitudes about the axis is opposite; larger finite strain ellipses occur beneath the eastern flank.

[20] The shear wave splitting is shown in Figures 4d–4f where the amount is calculated for a propagation distance of 20 km, in the local region of each aggregate. The presentation in Figures 4c and 4d is nonphysical in the sense that the splitting shown is the maximum possible in the spreading-parallel plane and, as indicated by the vectors, this direction varies significantly throughout the model space. A similar amount of splitting will occur at directions roughly 90° to the vector drawn in Figure 4d. (The wave surface plots by *Blackman et al.* [2002, Figure 7] illustrate this splitting behavior as well as the fact that rays traveling from out of the plane could accrue greater split times since the true maxima are often not in the plane.) For subsequent models we illustrate the splitting for specific incidence angles, but the plot of maximum shear wave

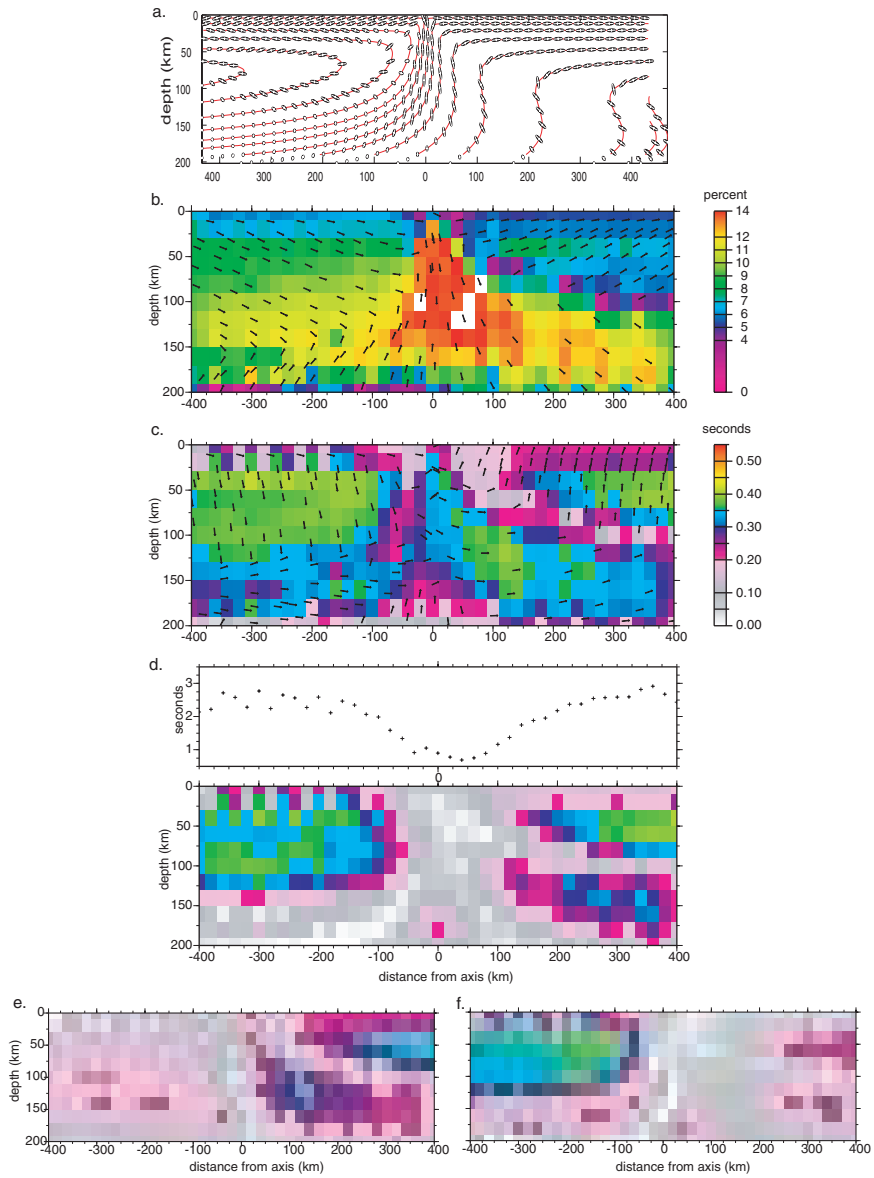

Figure 5. No vertical flow at 600 km model (section 3.2). (a) Streamlines and finite strain ellipses. (b) *P* wave anisotropy. (c) Maximum shear wave splitting. (d) Splitting for vertical incidence. (e) Local splitting for waves incident at 20° west of vertical. (f) Local splitting for waves incident at 20° east of vertical.

splitting nicely illustrates how the deformation field shapes the textural anisotropy. It is important to keep in mind that there are minima in shear wave splitting at angles roughly 45° to the maxima, and Figure 4e shows the large extent to which the delay between shear waves that accrues depends on ray path. For vertical incidence, we calculate average split times of 1 s on the eastern ridge flank, a minimum within 20 km of the axis, and average west flank splits of 0.75 s (Figure 4f). These surface splitting estimates are obtained by summing the local splitting in vertical slices of the model, down to the 200 km depth of the base.

3.2. Model With No Vertical Flow at 600 km Depth

[21] A more complete flow model simulates a viscosity contrast at the 660 km seismic discontinuity. Conder et al. (submitted manuscript, 2001)

developed a model where vertical velocities are zero at 600 km depth and horizontal velocities account for ridge migration, similar to the reference model above. Viscosity is pressure and temperature dependent. Material flows a significant distance to the east (in the ridge reference frame) before being entrained in the upwelling (Figure 5a). The texture calculation begins an arbitrary distance of 1000 km to the west of the spreading axis or at a depth of 200 km for streamlines that are deeper than that for a portion of the model.

[22] Texture develops as a result of the horizontal shear associated with ridge migration as well as the lack of vertical flow at the base of the model, which requires material to be drawn from the west to feed the ridge (Figure 5b). Beneath the west flank of the ridge, flow lines make a tight turn when the plate motion forces material from depth to change direction. The dominant velocity gradient in this region is du/dz (u, horizontal velocity; z, vertical direction), and the consistency of the fast P wave direction determined from the effective elastic constants for the texture model reflects this. Strong mineral alignment also occurs in the upwelling region and the maximum in-plane P wave anisotropy is determined there (Figure 5c), the fast axis is vertical. Interestingly, for shear waves traveling in the boundary-perpendicular plane, there is less shear wave splitting in the subaxial region than at similar depths off axis (Figure 5d). This is a function of the particular strain history of aggregates that move up through the subaxial zone versus those off axis (remember that out of plane splitting will be quite different).

[23] The maximum amount of shear wave splitting (Figure 5d) is somewhat greater to the west of the spreading axis, but when the splitting for a given incidence angle is computed (Figures 5e–5g), the surface signal varies considerably. For vertical incidence, the splitting predicted for the east and west flanks are similar, 2 s greater than the split times predicted at the axis. In contrast, there is significant asymmetry for incidence angles of 20° and the flank with greatest splitting switches with between east arriving rays and west arriving rays (Figures 5f and 5g).

[24] This flow model may begin to address some of the observed anisotropic structure in the MELT region [*Wolfe and Solomon*, 1998; *Forsyth et al.*, 1998b], but it cannot account for the heterogeneous velocity structure indicated in the seismic data [*Toomey et al.*, 1998; *Forsyth et al.*, 1998a; Conder et al., submitted manuscript, 2001]. Therefore additional means to achieve increased temperatures and melting beneath the western flank were pursued.

3.3. Pressure Gradient Model

[25] Conder et al. (submitted manuscript, 2001) propose that dynamic forces associated with the Pacific superswell [*McNutt*, 1998] could affect flow in the upper mantle for some distance. For the MELT area, they suggest this would result in a sustained pressure west of the axis that drives flow to east, in addition to the shear flow associated with migration of the spreading center. This model and the corresponding anisotropy are shown in Figure 6. Strong textures characterize the whole region within 400 km of the spreading axis (Figure 6b). The nature of the anisotropy is radically different from that determined for the case with no pressure gradient (Figure 5). The P wave anisotropy for this case is basically two-layered with higher degrees predicted for 100–200 km depths than for the shallower layer. Throughout the model, the fast P wave direction is subhorizontal although the sense of dip changes between the two ''layers.'' The maximum shear wave splitting does not vary that much throughout the model space, although vertically incident rays on the east flank accrue about half a second more splitting than those on the west flank (Figure 6d). The change in splitting across the axis is fairly sharp.

[26] This is an interesting model, and it is able to predict much of the velocity heterogeneity observed in the MELT region (Conder et al., submitted manuscript, 2001), but we find that the structure of the associated textural anisotropy does not agree with the observations. *Wolfe et al.,* [1998] find greater shear wave splitting on the west flank of the spreading center and *Forsyth et al.* [1998b] finds a reduction in the degree of anisotropy beneath the ridge axis. We cannot match the sense of these

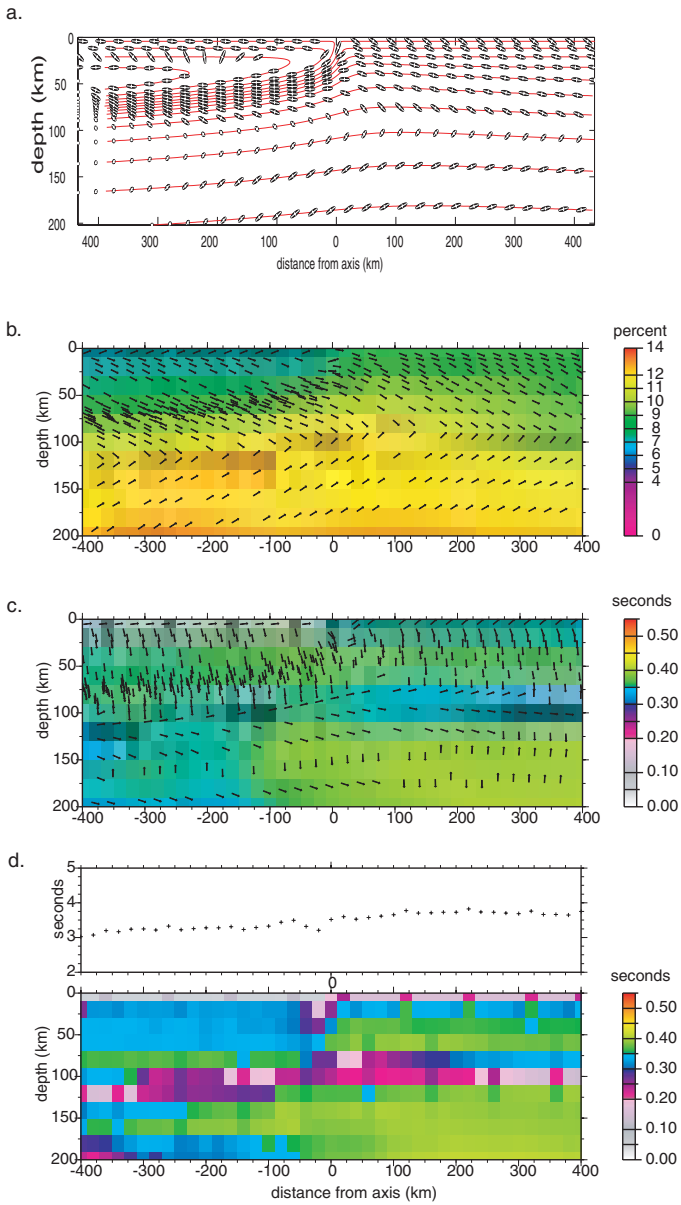

Figure 6. Pressure gradient, no vertical flow at 600 km model (Section 3.3). (a) Streamlines and finite strain ellipses. (b) *P* wave anisotropy. (c) Maximum shear wave splitting. (d) Splitting for vertical incidence.

observations with this model, even at other incidence angles.

3.4. Temperature Anomaly Model

[27] *Toomey et al.* [2002] favor a model in which the effect of the Pacific superswell is to raise temperatures to the west of the MELT region. The higher temperatures result in greater melting beneath the west flank and therefore asymmetric reduction in velocities, as observed [*Toomey et al.*, 1998; *Forsyth*, 1998b]. One of a series of their calculations is shown here (Figure 7a) to illustrate how the predicted anisotropy differs from the models shown in sections 3.1–3.3. Viscosity varies with pressure and temperature, so vertical flow at depth is reduced but not disallowed. Again, we begin texturing of randomly oriented 70:30 olivine:enstatite aggregates at 200 km depth and/or 1000 km distance from the ridge axis.

[28] Strong textures develop beneath the western flank and in the mid-depth region below the axis but

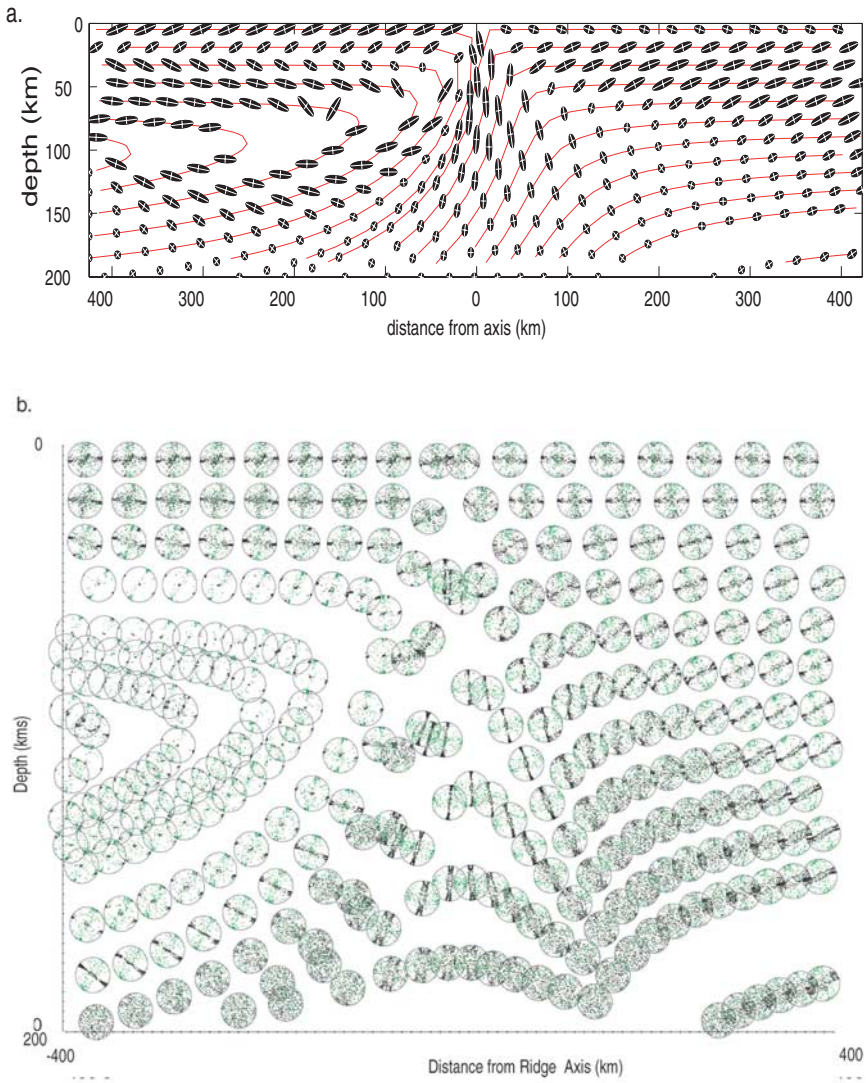

Figure 7. Temperature anomaly model (section 3.4). (a) Streamlines and finite strain ellipses. (b) The *a*-axis pole figures. (c) *P* wave anisotropy. (d) Maximum shear wave splitting. (e) Splitting for vertical incidence.

as the aggregates move through inflection points in the streamlines, some of this texture evolves to a more diffuse pattern as new principal strain directions take over (Figure 7b). *P* wave anisotropy is greatest at depth beneath the west flank as is the maximum amount of shear wave splitting. The direction of the fast *P* wave is subvertical below the ridge axis and is subhorizontal beneath the flanks. Similar to previous models (sections 3.1–3.3), the dip of the fast axis changes between shallower and deeper regions of the off-axis model.

[29] Shear waves with near-vertical incidence (SKS) are predicted to accrue just over 2 s of splitting on the west flank and to average a split of ~1 s on the east flank. The asymmetry in maximum shear wave splitting (Figure 7d) is strong enough that the west-east flank difference in amount of splitting holds for the range of incidence angles that would include teleseismic *S* waves (Figures 7e and 7f show the +/−20° incidence cases).

[30] This model provides the best agreement between the full set of MELT observations and the predicted anisotropic and heterogeneous velocity structure. Details of the anisotropic structure do vary with the depth assumed for the onset of texturing (where dislocation glide is assumed to take over

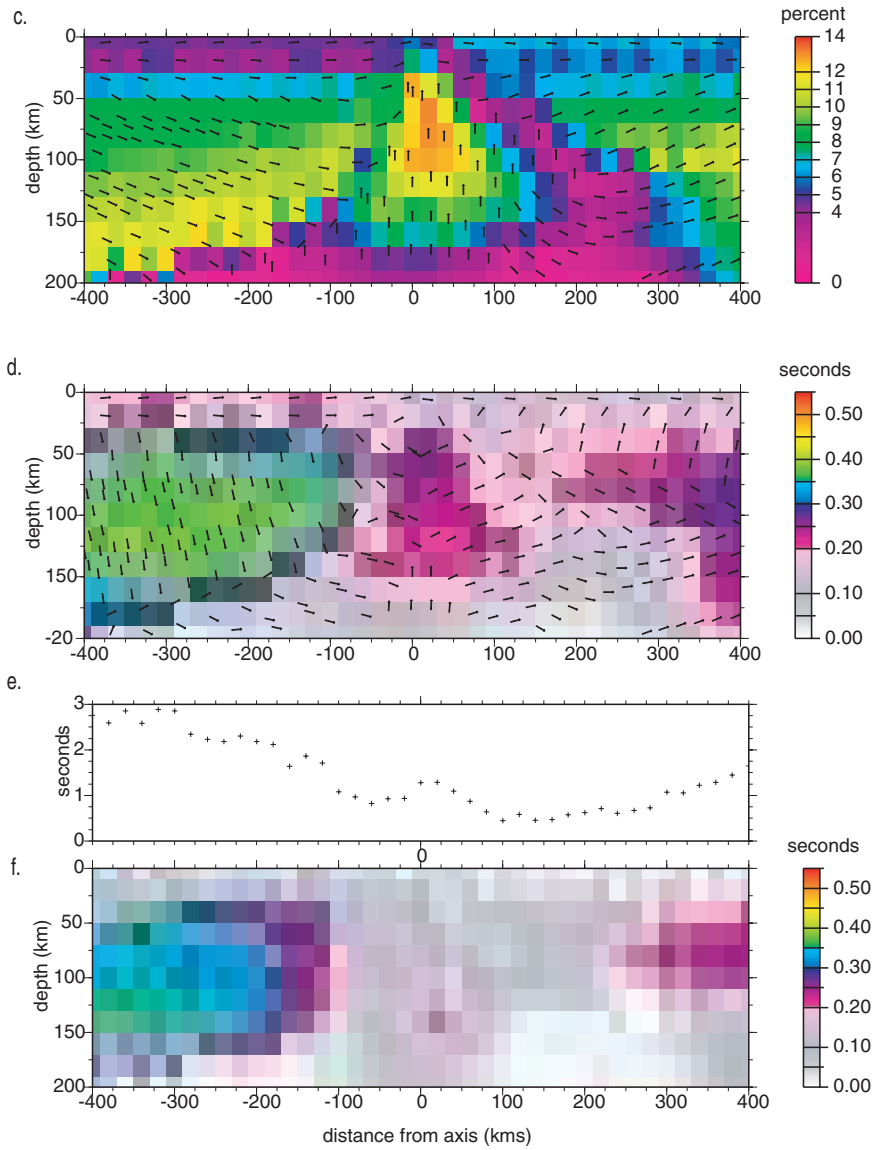

Figure 7. (continued)

from diffusion creep). A comparison of the predicted fast *P* directions based on our full texture calculations versus finitie strain is shown in Figure 8. The two methods produce similar results throughout much of the model space. However, there are 40–60 km wide regions below the base of the lithosphere and to the east of the rise axis in which the fast *P* directions disagree by more than 20°.

[31] We have focused on in-plane anisotropic structure thus far, but it is instructive to consider some of the out-of-plane predictions for this two-dimensional (2-D) flow model. Wave surface plots are shown for several locations of the *Toomey et al.* [2002] flow model (Figure 9). The *P* wave surfaces range from strong azimuthal distribution (with a fast direction and a girdle of slow directions at depth beneath the west flank), to a more orthorhombic signature (east of the spreading axis). There is significant variation in the pattern of shear wave splitting throughout the model space.

4. Three-Dimensional Flow Gradients

[32] Mantle flow within a few hundred kilometers of a plate boundary will almost always have at least

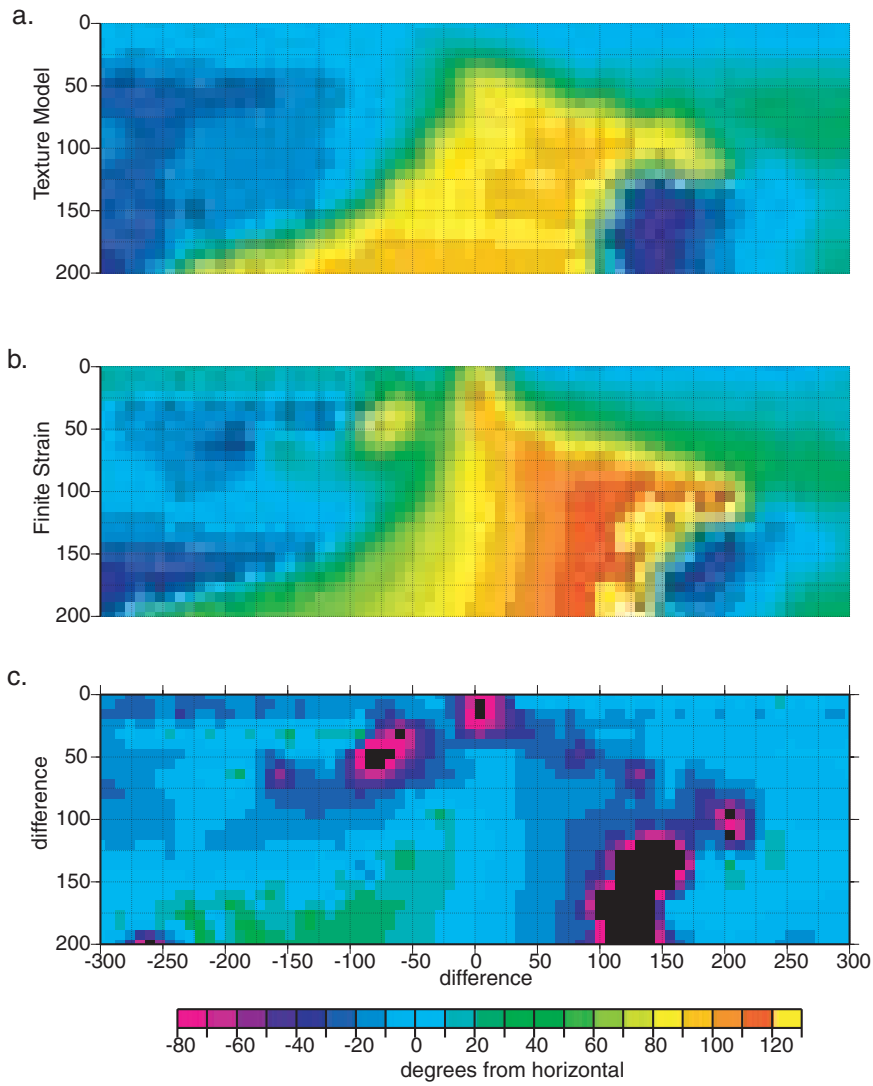

Figure 8. Comparison of predicted fast *P* wave directions for the temperature anomaly model. (a) Orientations (relative to horizontal) for the full texture calculation. (b) Orientations based on finite strain ellipse. (c) Difference between Figures 8a and 8b.

a small component of flow in the direction parallel to the strike of the boundary. At spreading centers this results from the fact that transform faults offset the ridge at intervals of 50–200 km [*Schouten et al.*, 1985] so that rates of upwelling decrease towards the offset [*Sleep and Biehler*, 1970; *Whitehead et al.*, 1984; *Crane*, 1985; *Parmentier and Phipps Morgan*, 1990]. In addition, the spreading center can migrate over the deeper mantle, and if its direction is out of the plane of relative plate motion, a component of along-axis flow results. Right or left lateral simple shear may characterize the uppermost mantle in the center of a long transform boundary but near its terminations more complex circulation will occur as the viscous mantle accommodates spatial variations in surface strain. Subduction zones are arcuate and the angle of relative plate motion often changes along the trench. Shear zones in the back arc region can also add a component of along-trench flow to the upper mantle wedge above the subducting plate. These three-dimensional (3-D) aspects of the flow will contribute to the alignment of anisotropic minerals. Indeed, fast polarization directions of shear waves measured along several subduction zones [e.g., *Fouch and Fischer*, 1996; *Brisbourne et al.*,

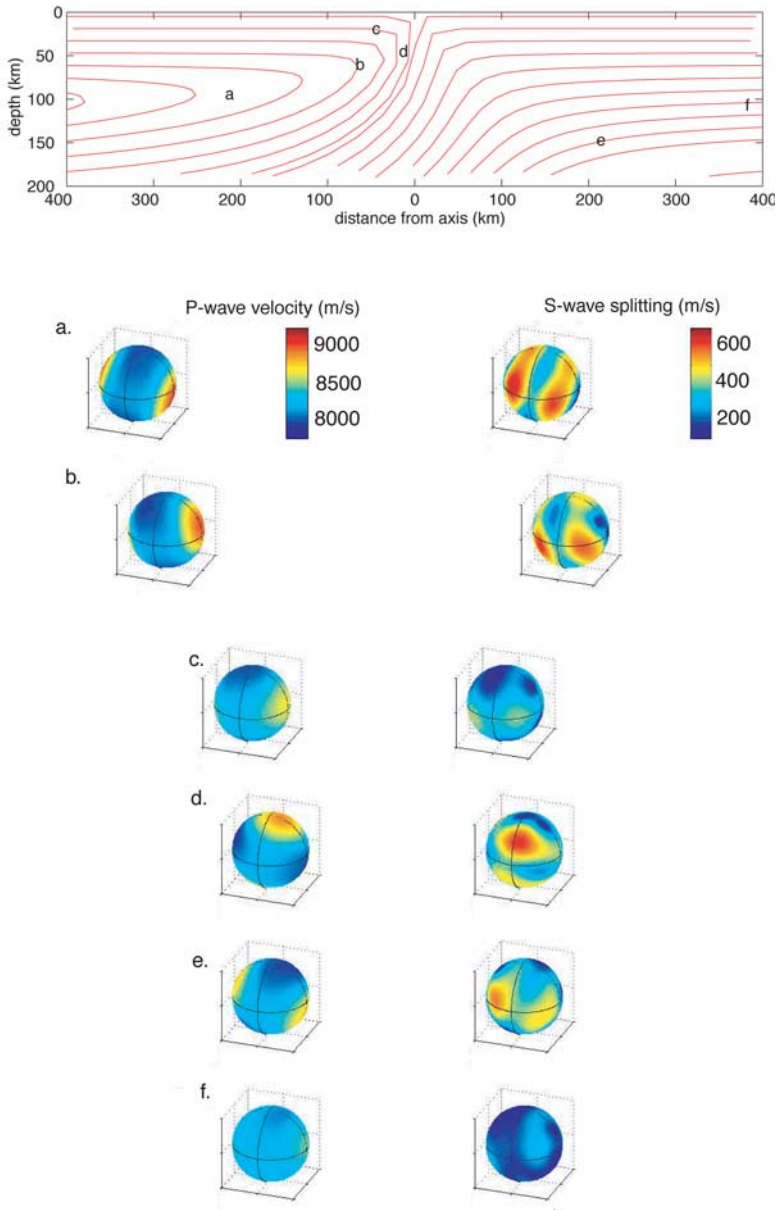

Figure 9. Wave surface plots for several local regions in the temperature anomaly model. Location of each wave surface plot is labeled on the streamline figure at top. Textures are shown in Figure 7b. Body waves in a medium with the corresponding (local) elastic tensor radiate from a spherical source at the center of each sphere. The spheres on the left illustrate the anisotropic *P* wave speeds, as a function of azimuth and incidence angle. The spheres on the right illustrate the amount of *S* wave splitting, as a function of azimuth and incidence angle.

1998] have been interpreted in terms of mantle flow along the strike of the down going plate. In this section we assess what flow gradients are required to modify the textures that develop in 2-D flow fields. In section 5 we show an example of textural evolution for more a complete 3-D flow field.

[33] A key factor for development of lattice preferred orientation is the size of the velocity gradients, the width or depth over which along-plate-boundary flow is significant, and the viscosity of the material being sheared, can be more important than the flow velocity itself. Two positions from within a passive plate spreading flow model are

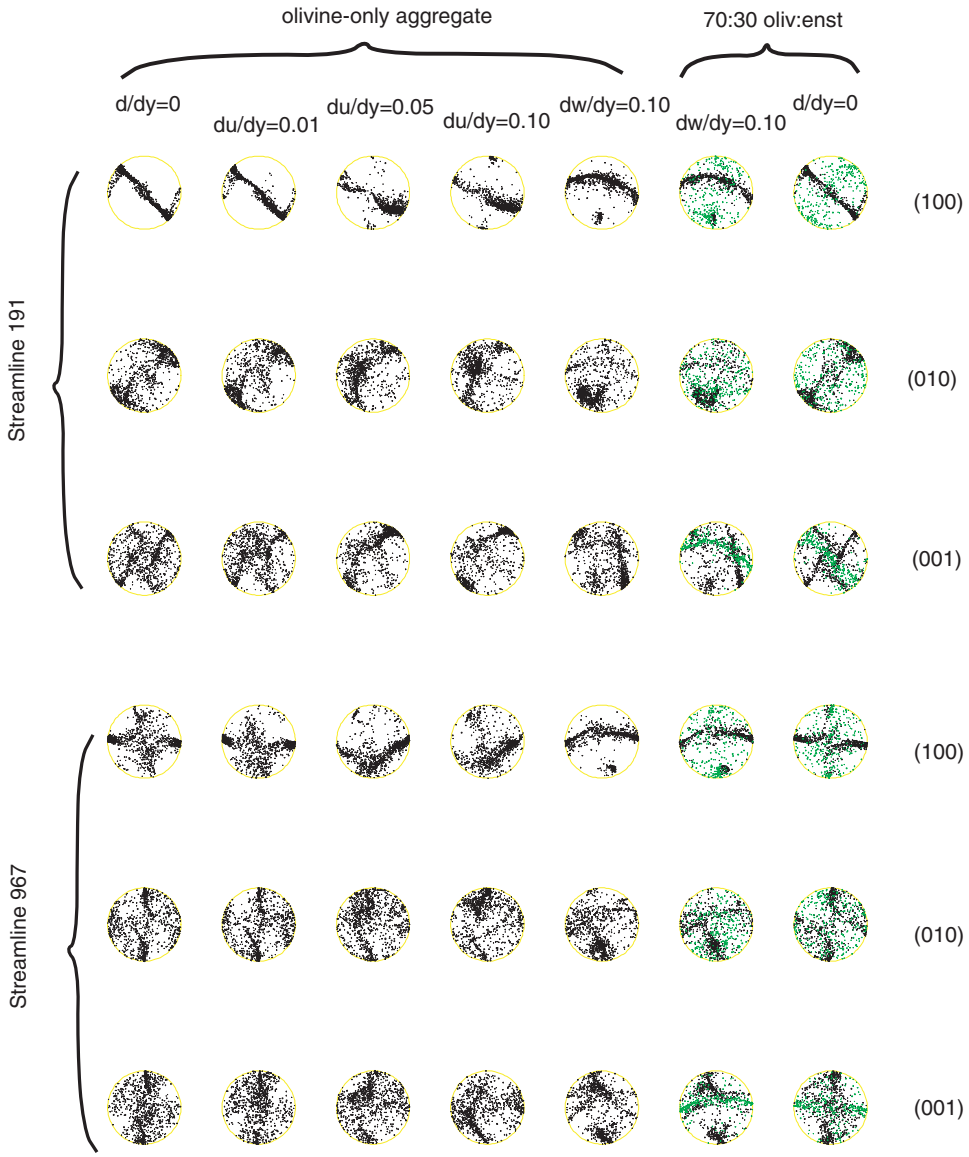

Figure 10. Effect of flow gradients in the third dimension on texture development. Equal area pole figures show texture for two streamlines from the model in Figure 1a. Streamline 191 has upwelling flow (only), a few kilometers from the spreading axis; streamline 967 upwells 20 km from the axis then follows the plate spreading at 20 km depth. Each set of poles corresponds to a different assumed third dimension gradient as labeled at top. A reference case with only 2-D flow is shown at left for olivine-only and at right for a 70:30 mix of olivine and enstatite.

used to illustrate the affect of 3-D velocity gradients on texturing. The u, v, and w flow velocity components correspond to the x (horizontal), y (out-of-plane), and z (vertical) directions, respectively. Figures 10 and 11 illustrate that the gradients in the third dimension need to be similar in size to the flow gradients in the boundary-perpendicular directions in order for the texture to be significantly modified from the 2-D distribution. For these 3-D cases we simply added a component of flow in the y direction to a previous set of streamline velocities and velocity gradients. A constant velocity gradient in the y direction was assumed for each case (for example, for a gradient of the horizontal velocity u in the y direction $du/dy = 0.1$). The aggregate experiences this third dimension of flow and any gradient of total velocity in this direction, in addition to the previously used 2-D deformation

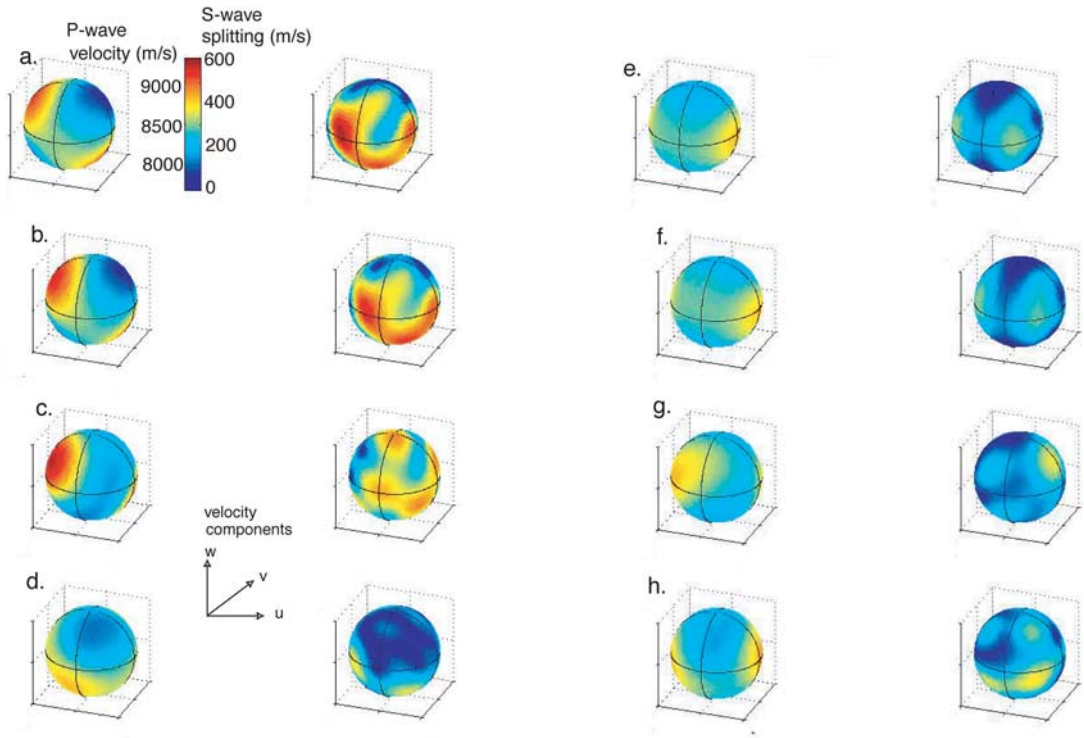

Figure 11. Wave surface plots illustrate how texture modifications due to flow gradients in the 3rd dimension can alter elastic behavior. Spheres on the left show *P* wave speeds; spheres on the right show *S* wave splitting (see Figure 9 caption). Corresponding textures for Figures 11a–11h are shown in Figure 10. (a) Streamline 191(sl191), 2D flow; (b) sl191, $du/dy = 0.01$; (c) sl191, $du/dy = 0.1$; (d) sl191, $dw/dy = 0.1$; (e) sl967, 2-D flow; (f) sl967, $du/dy = 0.01$; (g) sl967, $du/dy = 0.1$; and (h) sl967, $dw/dy = 0.1$.

field. The flow along a (now 3-D) streamline projects in 2-D to a line that is identical to that shown in Figure 1. The flow gradients in the 2-D model are of the order 0.1.

[34] The most significant effect of the along strike flow is to rotate the orientation distributions according to the imposed shear. The modifications to the effective elastic constants (aside from the rotation) result in only small changes in degree of *P* wave anisotropy (0.1–1%). The change in maximum shear wave splitting varies from the 2-D case by 5–10%, but, more importantly, the azimuthal dependence of splitting can be very different for 2-D versus 3-D flow (Figure 11).

5. Subduction and Back-Arc Shear Flow

[35] Convergent plate boundaries have mantle flow gradients that are similar in magnitude to those predicted within a few hundred kilometers of a spreading center. Many measurements of shear wave splitting indicate that seismic anisotropy is significant in the upper mantle between the downgoing and overriding plates (the mantle wedge). In some cases, the "fast direction" (the polarization direction determined for the fastest shear wave which is usually assumed to parallel the fast *P* wave direction) is parallel to the relative plate motion [*Bowman and Ando*, 1987; *Fischer and Wiens*, 1996; *Fouch and Fischer*, 1996]. However, in other areas, the fast direction aligns more along the strike of the plate boundary [*Russo and Silver*, 1994; *Brisbourne et al.*, 1998]. The latter has been interpreted to indicate that flow along the trench occurs. In this section we compare the anisotropic structure predicted for two simple models of flow at a subduction zone. The flow fields are taken from *Hall et al.* [2000] where shear wave splitting parameters were presented. Here we illustrate the

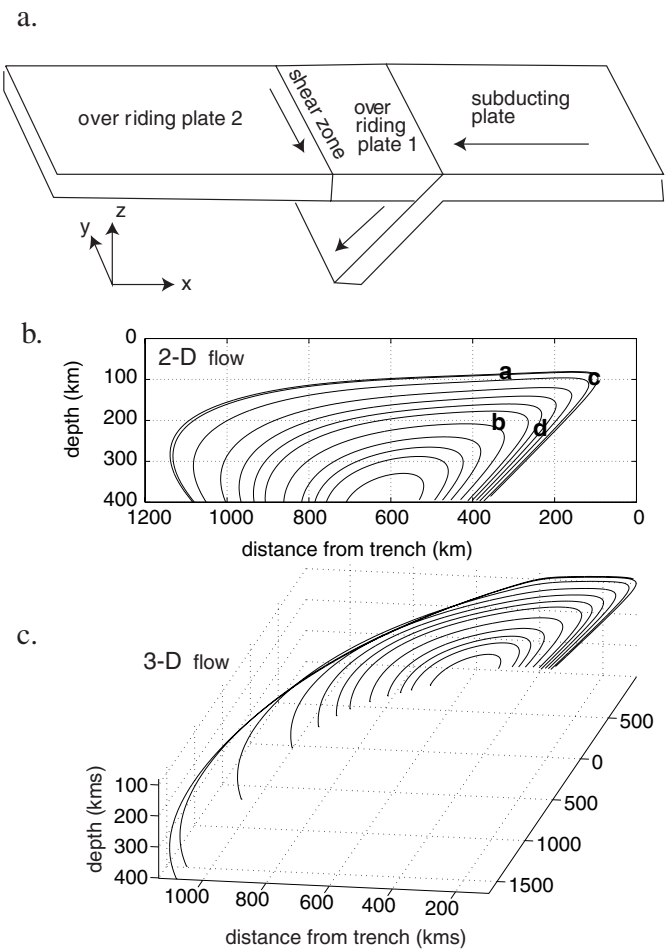

Figure 12. (a) Subduction flow model geometry [from *Hall et al.*, 2000]. (b) The 2-D models have no backarc shear, plate convergence drives the flow. Locations of wave surface plots in Figure 13 are labeled. When the shear zone is active, flow along the subduction zone is induced (c) and the velocity gradients influence the texture and seismic anisotropy.

nature of the anisotropy for a 2-D and a 3-D case in more detail.

[36] The trench perpendicular flow is induced by relative motion of the subducting and overiding plate (Figure 12; relative velocity is 90 mm/yr). Aggregates move along streamlines in a region 1000 km wide and 660 km deep. Texturing of 70:30 olivine:enstatite, 1000-grain aggregates begins when streamlines pass above a threshold depth. For the first 2-D case, a threshold depth of 400 km was used since some shear wave splitting measurements suggest the existence of anisotropy in the lower part of the mantle wedge [*Fouch and Fischer*, 1996]). We also compared this model with one in which texturing occurs only above 250 km, midway between the limits suggested by *Karato* [1992] for where deformation by diffusion creep is overtaken by dislocation driven crystal deformation.

[37] Strong texture develops in the upper part of the 400 km texturing threshold model, but as the aggregates encounter the tight corner near the trench, alternate slip systems are favored and the grains develop an orientation that subparallels the dip of the downgoing plate (Figure 13a). The strength of the subhorizontal alignment that developed in the upper mantle wedge is diffused somewhat in aggregates just above the subducting plate as the new strain field takes over. The strength of dip-subparallel texture increases with distance down slab but a thin layer of more complex texture remains and the fast *P* axes (Figure 13b) in this region are actually horizontal. This compromise between competing

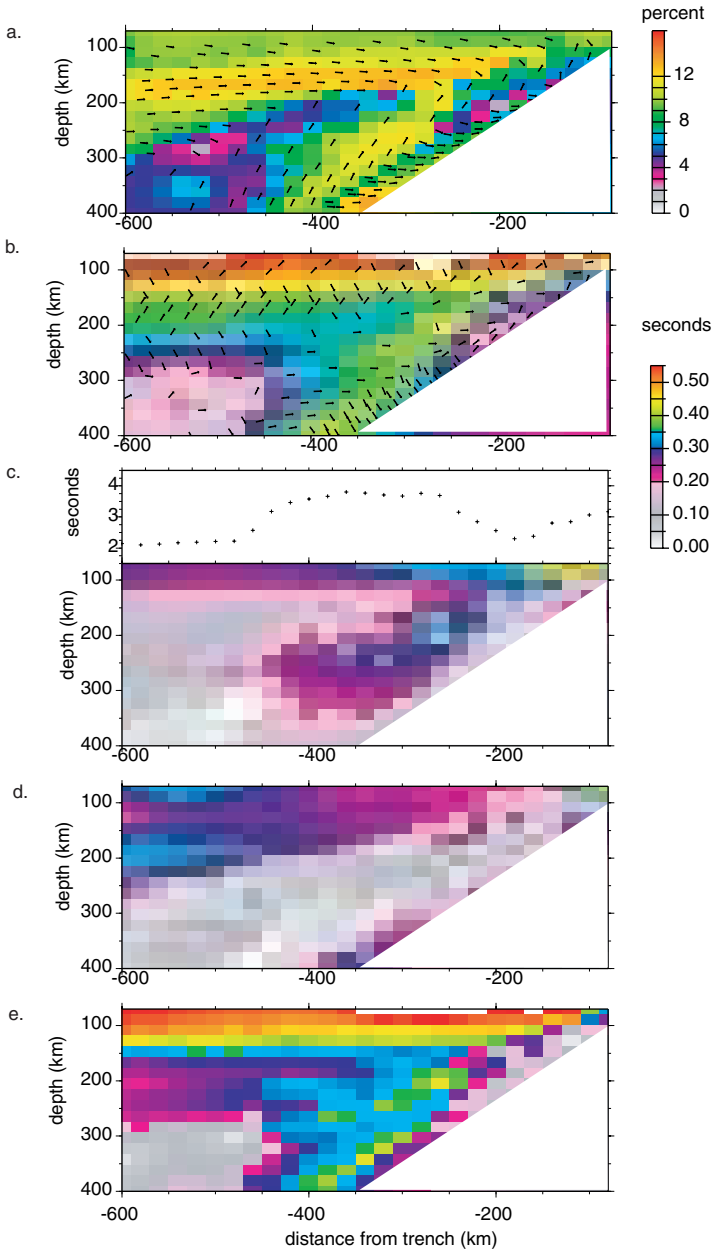

Figure 13. Predicted anisotropic structure for two-dimensional subduction model. (a) *P* wave anisotropy. (b) Maximum *S* wave splitting at local directions shown. (c) Splitting for vertically incident waves. (d) Local splitting for rays incident 20° west of vertical. (e) Local splitting for rays from the east at 20° incidence.

bipolar orientations just above the slab results in a thin layer of lower degree anisotropy for this model.

[38] Maximum shear wave splitting generally decreases with depth and with distance from the downgoing plate (Figure 13c). As for the spreading center models, the predicted splitting depends strongly on incidence angle. As expected, the split times for the 400 km threshold model are large (2–4 s for vertical incidence, Figure 13d). Rays incident from the west accrue up to 1.5 s splitting in the upper 130 km, whereas rays incident from the east do not split nearly as strongly (Figures 13e and 13f).

[39] Three-dimensional flow in the mantle wedge may be generated by a trench parallel shear in the back arc [*Hall et al.*, 2000] (Figure 12). Material is dragged by the plate, and this shearing affects the

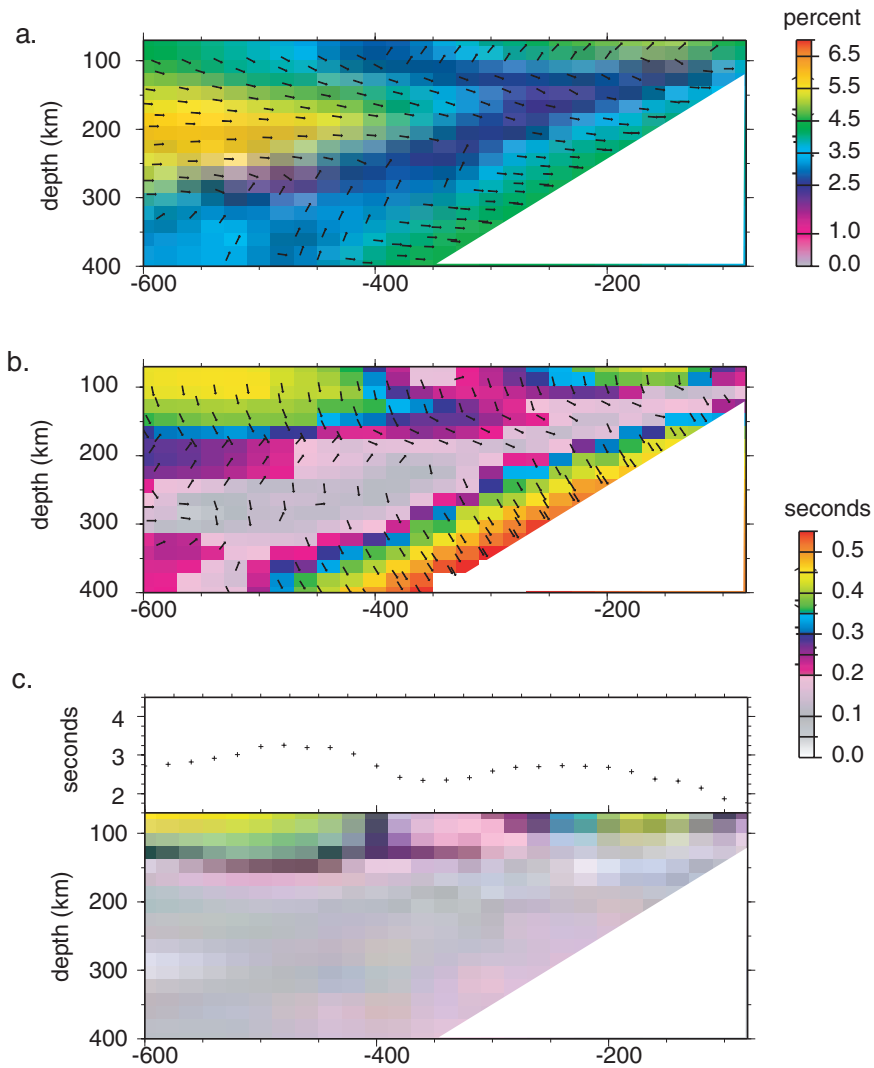

Figure 14. Predicted anisotropic structure for three-dimensional (3-D) subduction flow model. (a) *P* wave anisotropy in the plane of the model. (b) Maximum *S* wave splitting at the local directions shown. (c) *S* wave splitting for vertical incidence.

mineral alignment. Initially texture develops mainly in response to the plate convergence flow since streamlines begin 1000 km east of the surface subduction boundary, and the shear zone is located only 400 km from the boundary. The maximum flow rates along the trench in this model are just over 25% of the plate convergence rate (20 mm/yr). The associated shear is strong enough to rotate the textures noticeably (Figure 14a), but it cannot bring them into a trench parallel direction. Higher flow gradients would be required (section 2.4). For this model, the largest effect of the shear zone is to diffuse the strength of the convergence related *P* wave anisotropy (Figure 14b) and to eliminate the very high maximum shear wave splitting times in the upper 100 km of the model (Figure 14c). For vertically incident rays in the boundary-perpendicular plane, maximum delays between the fast and slow shear waves are just over 3 s for this 400 km texturing threshold model, with splits being lower to the east of the shear zone (Figure 14d).

[40] Although this is a fairly simple 3-D flow field, the predicted anisotropic structure differs markedly from the 2-D case. The surface signals are resolvably different between the two cases. As *Hall et al.* [2000] noted, the fast *P* directions predicted for this 3-D model do not rotate into a direction that is

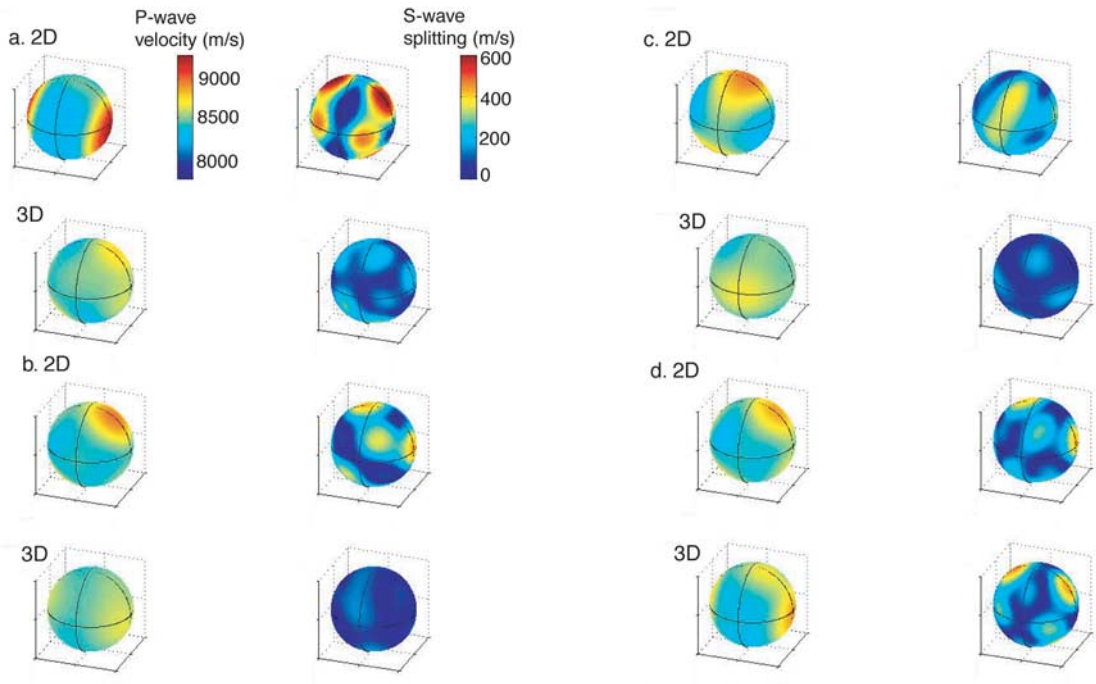

Figure 15. Wave surface plots illustrate the difference in local anisotropic structure that develops in 2-D versus 3-D subduction flow. Location of the examples are labeled a–d in Figure 12; for the 3-D case the location is projected onto the 2-D plane. Spheres on the left show *P* wave speeds; spheres on the right show *S* wave splitting.

trench parallel for most of the mantle wedge. Figure 15c shows one area in which it does, very close to the trench itself. Recent experimental results, however, may indicate that factors other than trench parallel flow are responsible for the measured directions of fast shear wave polarization. *Jung and Karato* [2001] find that the presence of water can significantly alter the anisotropic structure that develops during olivine deformation. Rather than aligning toward the shear plane in the direction of displacement, as occurs in dry olivine simple shear experiments, the *a* axes concentrate in a plane that is perpendicular to the displacement direction. If this behavior is representative of the mantle wedge material response to deformation, there would no longer be a need to invoke trench-parallel flow to explain fast directions that parallel the strike of the plate boundary. Additional studies are required to determine whether the experimental conditions capture the essential aspects for applying the results to the upper mantle near a subduction zone. At this point, the *Jung and Karato* [2001] results are mentioned as an important possibility but not yet as a firm constraint.

[41] When a threshold texturing depth of 250 km is used for the 2-D model, stronger texture is predicted for most of the upper mantle wedge. This occurs because the outer streamlines now begin texturing only after the turn in the flow at ~300 km depth, at a distance of 1000–1200 km from the trench. For the 400 km texturing threshold case, the preferred orientations that develop before this turn in the flow makes it more difficult for mineral axes to realign as consistently in the direction of surface plate motion. For the 250 km texturing threshold, the degree of *P* wave anisotropy and amount of shear wave splitting both decrease approximately monotonically with depth from the surface. Again, a region of reduced anisotropy occurs just above the down going slab. In addition to the expected reduction in shear wave splitting times, owing to the decreased thickness of the anisotropic region, this model predicts that split times are constant to the west of ~300 km distance from the trench. In contrast the model where texture begins at 400 km depth predicts that split times drop by 2 s between 300 and 350 km. The 250 km threshold model shows a monotonic increase in split time from the

trench to 300 km distance, whereas Figure 13c shows a decrease in splitting between the trench and 200 km distance, beyond which an increase to the west begins.

6. Discussion

[42] The models presented in sections 2–5 are intended to illustrate the scale and nature of variability in upper mantle anisotropic structure within 1000 km of a plate boundary. The flow and deformation parameters used are well within the range of currently accepted values. The fact that notable differences in the predicted anisotropic structure are determined for competing models is both encouraging and challenging. In order to discern patterns such as we predict, it is necessary to seismically resolve regions whose lateral scale is on the order of a few tens of km and whose thickness may be 20–50 km. Both vertical and lateral resolutions are important and sufficient azimuthal coverage could provide key constraints, not only on possible 3-D structure but for distinguishing between competing models of 2-D structure.

[43] Comparison between seismic anisotropy estimates based on finite strain and those based on direct texture calculations (sections 2.1 and 3.4) suggests that deformation associated with fairly simple flow fields produces finite strain ellipse orientations that match fast seismic directions determined for the texture models. In flow fields that are more complex, the two approaches to estimating anisotropy can differ significantly for portions of the model extending a few tens of kilometers. This occurs where a streamline undergoes more than one point of inflection. For example, in passive corner flow, there is a single point of inflection where upwelling transitions to plate-spreading flow. In our buoyuant model (section 2.1), the tight circulation region just off axis results in streamlines that have multiple inflection points where the sense of deformation changes significantly and strains are high. This is where the finite strain and texture estimates of anisotropy deviate. Similarly, the greatest deviations in the migrating spreading center, temperature anomaly model (section 3.4) are in the vicinity of the second (or subsequent) inflection in the flow lines. We conclude that finite strain provides a useful proxy for many situations but in the vicinity of plate boundaries, the possibility of complex flow should be assessed. If multiple, significant changes in flow direction are likely to occur within the study area then direct texture modeling may be required if the aim (and resolving capability) of the investigation is to address regions on the scale of a few to several tens of kilometers.

[44] We have not included possible recrystallization effects in the results presented here. In a companion paper [*Blackman et al.*, 2002], we apply the method of *Wenk and Tomé* [1999] to compute texturing of an olivine aggregate due to slip and recrystallization (grain growth and nucleation) along representative slow-spreading passive flow streamlines. Orientation distributions do differ, compared to deformation-only cases, and the corresponding seismic anisotropy varies between models but in a secondary rather than major way. The choice of model parameters employed for these recrystallization calculations follow those that produce a good match to laboratory and field observations for simpler deformation paths [*Wenk and Tomé*, 1999], but there are still significant uncertainties in their values. This is also the case for the method recently developed by *Kaminsky and Ribe* [2001]. These authors conclude that the change in orientation distributions, owing to recrystallization, with continued strain (beyond ~50%) is substantial and the olivine *a* axis maxima rotates into the shear plane. This is in agreement with results recently emerging from laboratory experiments [*Zhang and Karato*, 1995; *Zhang et al.*, 2000], but there are notable temperature, water content [*Jung and Karato*, 2001], and strain-rate dependencies that are only beginning to be characterized. In addition, along a streamline in a plate boundary flow field, the strain field varies significantly in both magnitude and principle axis direction, and there is not good documentation of how such variability (as opposed the experimentally applied progressive simple shear, for example) affects the behavior of polycrystalline rocks at mantle temperatures. Future experimental and field constraints are crit-

ical to continued progress along these lines. For now, we lean on the results given by *Blackman et al.* [2002] to infer that recrystallization in the types of flow fields that we discuss in sections 2–5 does not drastically change the structure of the anisotropy predicted for dislocation glide alone.

[45] Comparison of the four fast-spreading, migrating spreading center model results suggest that a number of observable features should allow discrimination between competing hypotheses of upper mantle flow near rifting plate boundaries. *Toomey et al.* [2002] and Conder et al. (submitted manuscript, 2001) discuss seafloor deepening, shear wave splitting (based on finite strain estimates of fast P and S polarization directions), and the fit of body wave travel times to those observed in the MELT data set from the East Pacific Rise 17°S. Our textural modeling corroborates their general findings and also illustrates some additional points. The regions for which finite strain estimates of fast *P* direction diverge from the direction determined for the full texture/elastic tensor analysis are not insignificant in size. The blue regions in Figure 8c are large enough to contribute to the overall *P* wave travel times. Similarly, the shear wave behavior in these regions would deviate from a finite strain-based estimate, and this would result in a somewhat altered pattern of *S* travel time and splitting measurements at the seafloor. The extent of the difference would depend on the incidence angle of the seismic waves. The pressure gradient model produces the greatest *P* wave anisotropy in the 150–200 km depth range; however, the inclination of the fast axis would serve to reduce the apparent horizontal versus vertical difference.

[46] It is clear that a full suite of seismic observations and detailed data analysis will be required if plate boundary mantle deformation fields are to be mapped with any certainty. A combination of teleseismic and regional source-receiver ranges will be necessary so that the range of incidence angles and turning depths is diverse. Local earthquakes and active source experiments [e.g., *Gaherty et al.*, 2001] would add important information on possible crustal variability and the nature of the sub Moho mantle. Integrated analysis of *P* and *S* body wave travel times and polarizations [*Schulte-Pelkum et al.*, 2001] as well as surface waves will be necessary. Three-dimensional arrays with groupings of closely spaced instruments, and total aperture on the order of a few hundred kilometers will be required. In addition to comprehensive data analysis, tomographic inversion results should be guided by forward modeling of the development of anisotropic structure so that biases introduced by necessary simplifications in parameterization are understood and incorporated in the interpretation of results. Fortunately, we are now in a good position to achieve many of these goals in the coming decade with the current rapid growth in instrument availability, reliability and seafloor longevity and increased computational sophistication for analysis and modeling.

Acknowledgments

[47] Flow model results or streamline information calculated by James Conder, Doug Toomey, and Chad Hall were used for some of the models presented in this paper, and we appreciate their generosity in providing these field data and the many discussions on this topic over the past 2 years. Reviews by Greg Hirth, Neil Ribe, and Peter Kelemen were quite helpful for clarifying our results and better emphasizing their context. We appreciate these colleagues input and patience in wading through both this and the companion manuscript. Blackman was supported by NSF for this work under grant OCE98-12560.

References

Anderson, O. L., and D. B. Isaak, Elastic constants of mantle minerals at high temperature, in *Global Earth Physics: A Handbook of Physical Constants, AGU Reference Shelf Ser.*, vol. 1, edited by T. J. Ahrens, AGU, Washington, D.C., 1995.

Blackman, D. K., Variation in lithospheric stress along ridge-transform plate boundaries, *Geophys. Res. Lett.*, *24*, 461–464, 1997.

Blackman, D. K., J.-M. Kendall, P. R. Dawson, H.-R. Wenk, D. Boyce, and J. Phipps Morgan, Teleseismic imaging of subaxial flow at mid-ocean ridges: Travel-time effects of anisotropic mineral texture in the mantle, *Geophys. J. Int.*, *127*, 415–426, 1996.

Blackman, D. K., H.-R. Wenk, and J.-M. Kendall, Seismic anisotropy of the upper mantle, 1, Factors that affect mineral texture and effective elastic properties, *Geochem. Geophys. Geosyst.*, *3*(9), 10.1029/2001GC000248, 2002.

Bowman, J. R., and M. Ando, Shear-wave splitting in the upper-mantle wedge above the Tonga subduction zone, *Geophys. J. Int.*, *88*, 25–41, 1987.

Brisbourne, A., G. W. Stuart, and J.-M. Kendall, Anisotropic structure of the Hikurangi subduction zone, New Zealand: Integrated interpretation of surface-wave and body-wave observations, *Geophys. J. Int.*, *137*, 214–230, 1998.

Buck, W. R., and W. Su, Focused mantle upwelling below mid-ocean ridges due to feedback between viscosity and melting, *Geophys. Res. Lett.*, *16*, 641–644, 1989.

Carter, N. L., Steady state flow of rock, *Rev. Geophys.*, *14*, 301–360, 1976.

Chastel, T. B., P. R. Dawson, H.-R. Wenk, and K. Bennett, Anisotropic convection with implications for the upper mantle, *J. Geophys. Res.*, *98*, 17,575–17,771, 1993.

Cochran, J. R., Variations in subsidence rates along intermediate and fast spreading mid-ocean ridges, *Geophys. J. R. Astron. Soc.*, *87*, 421–454, 1986.

Crane, K., The spacing of ridge axis highs: dependence upon diapiric processes in the underlying asthenosphere?, *Earth Planet. Sci. Lett.*, *72*, 405–414, 1985.

Davis, E. E., and J. L. Karsten, On the cause of the asymmetric distribution of seamounts about the Juan de Fuca Ridge; ridge-crest migration over a heterogeneous asthenosphere, *Earth Plant. Sci. Lett.*, *79*, 385–396, 1986.

Dawson, P. R., and H.-R. Wenk, Texturing of the upper mantle during convection, *Philos. Mag. A*, *80*, 573–598, 2000.

Fischer, K. M., and D. A. Wiens, The depth distribution of mantle anisotropy beneath the Tonga subduction zone, *Earth Planet. Sci. Lett.*, *142*, 253–260, 1996.

Forsyth, D. W., The early structural evolution and anisotropy of the oceanic upper mantle, *Geophys. J. R. Astron. Soc.*, *43*, 103–162, 1975.

Forsyth, D. W., et al., Imaging the deep seismic structure beneath a mid-ocean ridge: The MELT Experiment, *Science*, *218*, 1215–1218, 1998a.

Forsyth, D. W., S. C. Webb, L. M. Dorman, and Y. Shen, Phase velocities of Rayleigh waves in the MELT experiment on the East Pacific Rise, *Science*, *280*, 1235–1238, 1998b.

Fouch, M. J., and K. M. Fischer, Mantle anisotropy beneath Northwest Pacific subduction zones, *J. Geophys. Res.*, *101*, 15,987–16,002, 1996.

Gaherty, J. B., D. Lizarralde, J. A. Collins, and G. Hirth, Far-offset airgun imaging of the mantle: lithospheric anisotropy of the North Atlantic, *Eos Trans. AGU*, *82*(47), F1113, Fall Meet. Suppl., 2001.

Guest, W. S., and J.-M. Kendall, Modelling waveforms in anisotropic inhomogeneous media using ray and Maslov theory: Applications to exploration seismology, *Can. J. Explor. Geophys.*, *29*, 78–92, 1993.

Hall, C. E., K. M. Fischer, E. M. Parmentier, and D. K. Blackman, The influence of plate motions on three-dimensional back-arc mantle flow and shear wave splitting, *J. Geophys. Res.*, *105*, 28,009–28,034, 2000.

Hess, H. H., Seismic anisotropy of the uppermost mantle under the oceans, *Nature*, *203*, 629–631, 1964.

Jung, H., and S. Karato, Water-induced fabric transitions in olivine, *Science*, *293*, 1460–1463, 2001.

Kaminski, E., and N. M. Ribe, A kinematic model for recrystallization and texture development in olivine polycrystals, *Earth Planet. Sci. Lett.*, *189*, 253–267, 2001.

Karato, S., On the Lehmann discontinuity, *Geophys. Res. Lett.*, *19*, 2255–2258, 1992.

Karato, S., and P. Wu, Rheology of the upper mantle-A synthesis, *Science*, *260*, 771–778, 1993.

Kumazawa, M., The elastic constants of single-crystal orhopyroxene, *J. Geophys. Res.*, *74*, 5973–5980, 1969.

Mainprice, D., G. Barroul, and W. Ben Ismaïl, The seismic anisotropy of the Earth's mantle: From single crystal to polycrystal, in *Earth's Deep Interior, AGU Monogr. Ser.*, vol. 117, edited by S. i. Karata et al., pp. 237–264, AGU, Washington, D.C., 2000.

McKenzie, D., Finite deformation during fluid flow, *Geophys. J. R. Astron. Soc.*, *58*, 689–715, 1979.

McNutt, M. K., Superswells, *Rev. Geophys.*, *36*, 211–244, 1998.

Nicolas, A., and N. I. Christensen, Formation of anisotropy in upper mantle peridotites-A review, in *Composition, Structure and Dynamics of the Lithosphere-Asthenosphere System*, Geodyn. Ser., vol. 16, edited by K. Fuchs and C. Froidevaux, AGU, Washington, D.C., 1987.

Nicolas, A., and J. P. Poirier, *Crystalline Plasticity and Solid-State Flow in Metamorphic Rocks*, John Wiley, New York, 1976.

Nishimura, C. E., and D. W. Forsyth, The anisotropic structure of the upper mantle in the Pacific, *Geophys. J. Int.*, *96*, 203–229, 1989.

Parmentier, E. M., and J. Phipps Morgan, Spreading rate dependence of three-dimensional structure in oceanic spreading centres, *Nature*, *348*, 325–328, 1990.

Raitt, R. W., G. G. Shor, T. J. G. Francis, and G. B. Morris, Anisotropy of the Pacific upper mantle, *J. Geophys. Res.*, *74*, 3095–3109, 1969.

Rea, D. K., Model for the formation of topographic features of the East Pacific Rise crest, *Geology*, *3*, 77–80, 1975.

Ribe, N. M., Seismic anisotropy and mantle flow, *J. Geophys. Res.*, *94*, 4213–4223, 1989.

Ribe, N. M., On the relation between seismic anisotropy and finite strain, *J. Geophys. Res.*, *97*, 8737–8747, 1992.

Ribe, N. M., and Y. Yu, A theory for the evolution of orientation textures in deformed olivine polycrystals, *J. Geophys. Res.*, *96*, 8325–8335, 1991.

Russo, R. M., and P. G. Silver, Trench-parallel flow beneath the Nazca plate from seismic anisotropy, *Science*, *263*, 1105–1111, 1994.

Scheirer, D. S., D. W. Forsyth, M.-H. Cormier, and K. C. Macdonald, Shipboard geophysical indications of asymmetry and melt production beneath the East Pacific Rise near the MELT experiment, *Science*, *280*, 1221–1224, 1998.

Schouten, H., K. D. Klitgord, and J. A. Whitehead, Segmentation of mid-ocean ridges, *Nature*, *317*, 225–229, 1985.

Schulte-Pelkum, V., G. Masters, and P. M. Shearer, Upper mantle anisotropy from long-period P polarization, *J. Geophys. Res.*, *106*, 21,917–21,934, 2001.

Shearer, P., and J. A. Orcutt, Anisotropy in the oceanic lithosphere-Theory and observations from the Ngendei seismic refraction experiment in the south-west Pacific, *Geophys. J. R. Astron. Soc.*, *80*, 493–526, 1985.

Shimamura, H., Anisotropy in the oceanic lithosphere of the Northwestern Pacific basin, *Geophys. J. R. Astron. Soc.*, *76*, 253–260, 1984.

Silver, P. G., Seismic anisotropy beneath the continents-probing the depths of geology, *Ann. Rev. Earth Planet. Sci.*, *24*, 385–432, 1996.

Silver, P. G., and W. W. Chan, Shear wave splitting and subcontinental mantle deformation, *J. Geophys. Res.*, *96*, 16,429–16,454, 1991.

Sleep, N. H., and S. Biehler, Topography and tectonics at the intersection of fracture zones with central rifts, *J. Geophys. Res.*, *75*, 2748–2752, 1970.

Sleep, N. H., and B. R. Rosendahl, Topography and tectonics of mid-oceanic ridge axes, *J. Geophys. Res.*, *84*, 6831–6839, 1979.

Smith, W. H. F., and P. Wessel, Gridding with continuous curvature splines in tension, *Geophysics*, *55*, 293–304, 1990.

Sotin, C., and E. M. Parmentier, Dynamical consequences of compositional and thermal density stratification beneath spreading centers, *Geophys. Res. Lett.*, *16*, 835–838, 1989.

Stein, S., H. J. Melosh, and J. B. Minster, Ridge migration and asymmetric sea-floor spreading, *Earth Planet. Sci. Lett.*, *36*, 51–62, 1977.

Tommasi, A., D. Mainprice, G. Cannova, and Y. Chastel, Viscoplastic self-consistent equilibrium modeling of olivine lattice preferred orientations: Implications for the upper mantle seismic anisotropy, *J. Geophys. Res.*, *105*, 7893–7908, 2000.

Toomey, D. R., W. S. D. Wilcock, S. C. Solomon, W. C. Hammond, and J. A. Orcutt, Mantle seismic structure beneath the MELT region of the East Pacific Rise from P and S wave tomography, *Science*, *280*, 1224–1227, 1998.

Toomey, D. R., W. S. D. Wilcock, J. A. Conder, D. W. Forsyth, J. Blundy, E. M. Parmentier, and W. C. Hammond, Asymmetric mantle dynamics in the MELT region of the East Pacific rise, *Earth Planet. Sci. Lett.*, *200*, 287–295, 2002.

Turcotte, D. L., and J. Phipps Morgan, The physics of magma migration and mantle flow beneath a mid-ocean ridge, in *Mantle Flow and Melt Generation at Mid-Ocean Ridges, Geophys. Monogr. Ser.*, vol. 71, edited by J. Phipps Morgan, D. K. Blackman, and J. M. Sinton, pp. 155–182, AGU, Washington, D.C., 1992.

Wenk, H.-R., and C. N. Tomé, Modeling dynamic recrystallization of olivine aggregates deformed in simple shear, *J. Geophys. Res.*, *104*, 25,513–25,527, 1999.

Wenk, H.-R., K. Bennett, G. R. Canova, and A. Molinari, Modelling plastic deformation of peridotite with the self-consistent theory, *J. Geophys. Res.*, *96*, 8337–8349, 1991.

Whitehead, J. A., H. J. B. Dick, and H. Schouten, A mechanism for magmatic accretion under spreading centres, *Nature*, *312*, 146–148, 1984.

Wolfe, C. J., and S. C. Solomon, Shear-wave splitting and implications for mantle flow beneath the MELT region of the East Pacific Rise, *Science*, *280*, 1230–1232, 1998.

Zhang, S., and S. Karato, Lattice preferred orientation of olivine deformed in simple shear, *Nature*, *375*, 774–777, 1995.

Zhang, S., S. Karato, J. Fitz Gerald, U. H. Faul, and Y. Zhou, Simple shear deformation of olivine aggregates, *Tectonophysics*, *316*, 133–152, 2000.